An Investigation into Transmission Line Radiation

By

MATTHEW KYLE ROTH

Bachelor of Science in Electrical Engineering
Oklahoma State University
Stillwater, Oklahoma
2021

Submitted to the Faculty of the
Graduate College of the
Oklahoma State University
in partial fulfillment of
the requirements for
the Degree of
MASTER OF SCIENCE
May, 2023

An Investigation into Transmission Line Radiation

Thesis Approved:

Dr. James West

Thesis Advisor

Dr. Charles Bunting

Dr. Daquing Piao

ACKNOWLEDGMENTS

I would like to express my sincere gratitude to Dr. James West, my thesis advisor, for his invaluable guidance, encouragement, and unwavering support throughout my research journey. His expertise, insightful feedback, and unwavering dedication were instrumental in shaping the direction and quality of this thesis.

I would also like to extend my appreciation to Dr. Charles Bunting and Dr. Daquing Piao, my committee members, for their valuable feedback and insightful suggestions that helped me refine my work and improve its overall quality.

I am also deeply grateful to my parents, friends, and family for their unwavering love, support, and encouragement throughout my academic journey. Their constant encouragement and support were a source of motivation, inspiration, and strength during challenging times.

I also want to give a shout-out to my lab mates, who made the long hours in the lab more bearable with their witty banter. Their eclectic taste in music, endless quick meal runs, and shared struggles over finicky equipment were all part of what made this thesis possible. I am grateful for their camaraderie and the memories we shared, both the good and the bad (mostly the good, though). Thank you for being an awesome bunch!

Lastly, I would like to thank all the individuals who contributed to this thesis, whether through their feedback, encouragement, or other forms of support. Your contributions were invaluable in helping me complete this work.

Acknowledgments reflect the views of the author and are not endorsed by committee members or Oklahoma State University.

Name: MATTHEW KYLE ROTH

Date of Degree: MAY, 2023

Title of Study: AN INVESTIGATION INTO TRANSMISSION LINE RADIATION

Major Field: ELECTRICAL ENGINEERING

Abstract:

An empirical study has been performed to investigate the radiation mechanisms that yield emissions from two-conductor transmission line circuits at microwave frequencies up to 8.5 GHz. The measured signal levels established by radiation from the test configurations within a reverberation chamber were compared with the levels radiated by a wideband dual-ridge antenna in the same environment. Three basic test configurations were considered, one in which the transmission line segment and full feed structure, including balun and feed plate, were contained within the chamber cavity, one in which the feed structure and feed plate could be isolated from the cavity, and a third with two distinct environments measurements of radiation from the feed structure and feed plate as well as radiation from the transmission line could be performed simultaneously.

The measurements show that radiation from the line terminations dominates the emission within the cavity that contains it, including when only bulkhead SMA pin adapters were exposed to the cavity, independent of whether the line was a parallel-conductor, twin-lead line, or a twisted pair. Measured emissions from the two lines were only consistent with transmission line theory when the lines were passed through apertures in the chamber walls. The results suggest that the emissions can be modeled by adding a radiation resistance element at the connector location to standard transmission line theory.

TABLE OF CONTENTS

LIST OF TABLES

LIST OF FIGURES

CHAPTER I

Introduction

Systems in use all around us are becoming more complex, more technologically advanced, and more sensitive. Boats, cars, planes, and especially spacecraft are overrun with sensitive instrumentation that could have very costly consequences in the event of a failure. Despite the meticulous care taken to shield the environment these electronics live in, high-frequency energy can still couple into the otherwise electromagnetically isolated environment through power and low-frequency signal wire penetrations. A high frequency field can induce currents onto the cables that flow through the wall penetration and reradiate inside the shielded environment. Operating at frequencies much higher than intended, it can be hard to prevent this field from coupling unless properly anticipated. In a situation where these cables allow interaction between two environments with closed reverberant cavities, it's possible to establish strong standing waves inside these chambers and produce very high field levels.

As communications technologies have been reaching into higher and higher frequencies, this problem has arisen and will continue to worsen unless taken into account while designing systems. Therefore, it is essential to understand the mechanisms of energy coupling and to develop models to predict and mitigate the effects of electromagnetic interference. This paper aims to do just that by presenting a transmission line model that represents the radiation behavior along the line, a numerical method to calculate the per-unit-length parameters of a transmission line at and at terminations, and outlining an experimental effort conducted to validate these models as well as investigate the various radiation mechanisms of a transmission line.

1.1 Outline

Chapter II starts by outlining the classical transmission line model and the per-unit-length parameters needed to apply the telegrapher's equations. This sets the foundation for the transmission line model outlined in the later part of the chapter to represent radiation losses. In chapter III, the mathematical method behind calculating the per-unit-length parameters from chapter II is further analyzed. This chapter applies this math to a finite element solver, FreeFEM++[4], and describes the steps in practically calculating the per-unit-length parameters for an arbitrary transmission line structure. At the end of this chapter, this per-unit-length solver is validated against some analytic models to ensure accuracy. Chapter IV will present further validation of both the finite element code and the transmission line model in the form of scattering parameter measurements of two transmission line structures in a fully anechoic chamber. This chapter also shows the experimental investigation performed while trying to isolate radiating mechanisms of transmission line assemblies using reverberation chambers. Chapter V will present conclusions and suggest further work to be done.

CHAPTER II

Background

The goal of this work was to determine, and hopefully mathematically represent, the mechanisms of radiation on a transmission line. This is controlled by transmission line theory's telegrapher's equations and the per-unit-length parameters. In this chapter, we will take a look at the classical representation of telegrapher's equations, have an overview of their derivation, and talk about methods used to modify transmission line theory to represent radiation. We will also go over the specific transmission line method that was implemented in this study.

2.1 Classical Transmission Line Theory

This section will go over the derivation of classical transmission line theory and the per-unit-length parameters contained within. In order to extend the telegrapher's equations to represent radiation, it's first important to understand how to mathematically arrive at their classical form. From this, the derivation can be altered to account for radiation loss mechanisms.

For this derivation, we will take a simple transmission line model, make some assumptions, and see the transmission line equations can be quickly derived in their typical form. Clayton Paul has a more detailed and complete explanation of this derivation in [8, Chapter 2].

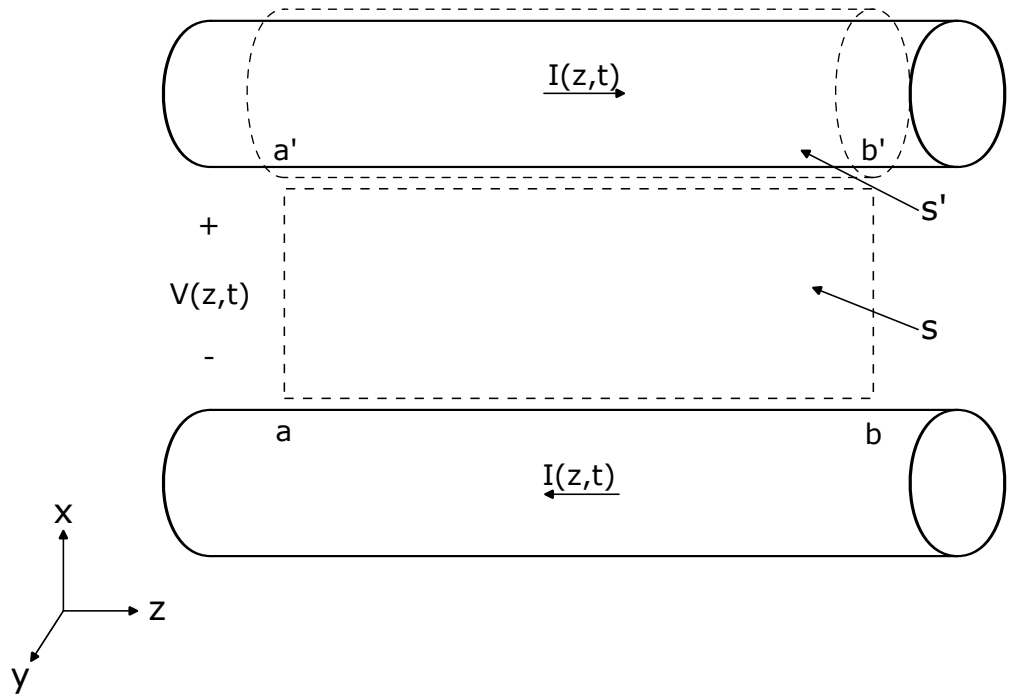

Figure 1: Two wire, straight, uncoated transmission line structure for transmission line theory derivation

2.1.1 Derivation from Maxwell's Equations

The exact conductor shape for this transmission line does not greatly affect the following derivation. The situation to be derived is shown in figure 1, a straight twin-lead line with uncoated conductors has been chosen to make visualizing easier for the reader. This line has two conductors extending alone the x-axis and the line is transverse to z-axis.

From Faraday's law, we can form a closed contour integral around a surface, s, extending between the two conductors:

$$\oint_c \mathcal{E} \cdot \mathbf{dl} = -\mu \frac{d}{dt} \int_s \mathcal{H} \cdot \mathbf{ds} \tag{2.1.1}$$

$$\int_a^{a'} \mathcal{E}_t \cdot \mathbf{dl} + \int_{a'}^{b'} \mathcal{E}_1 \cdot \mathbf{dl} + \int_{b'}^{b} \mathcal{E}_t \cdot \mathbf{dl} + \int_b^{a'} \mathcal{E}_1 \cdot \mathbf{dl} = \mu \frac{d}{dt} \int_s \mathcal{H}_t \cdot \mathbf{a}_n ds \tag{2.1.2}$$

Some assumptions can be made to simplify this equation. First, by assuming a TEM field

on the transmission line structure, the integrals between conductors can be written simply as a time and z dependent voltage. Second, defining a per-unit-length resistance on the wires, the integrals along the length of the wires can be written using Ohm's law. Applying these two simplifications, the closed contour integral from (2.1.2) can then be written as:

$$-V(z,t) + r_1 \Delta z I(z,t) + V(z+\Delta z,t) + r_0 \Delta z I(z,t) = \mu \frac{d}{dt} \int_s \mathcal{H}_t \cdot \mathbf{a}_n ds \tag{2.1.3}$$

A per-unit-length magnetic flux penetrating the top conductor can be written as:

$$-\mu \lim_{\Delta z \to 0} \frac{1}{\Delta z} \int_s \mathcal{H}_t \cdot \mathbf{a}_n ds = l I(z,t) \tag{2.1.4}$$

After rearranging (2.1.3), substitution of the per-unit-length magnetic flux from (2.1.4), and taking the limit as $z \to 0$, the first transmission line equation is:

$$\frac{dV(z,t)}{dz} = -rI(z,t) - l\frac{dI(z,t)}{dt} \tag{2.1.5}$$

Now, place a closed cylindrical surface, s', around the top conductor. From the equation of conservation of charge:

$$\oiint_{s'} \mathcal{J} \cdot \mathbf{ds}' = -\frac{d}{dt} Q_{enc} \tag{2.1.6}$$

Writing this out over the end caps, s'_e, and the sides, s'_s, gives two integrals:

$$\iint_{s'_e} \mathcal{J} \cdot \mathbf{ds}' = I(z+\Delta z,t) - I(z,t) \tag{2.1.7}$$

$$\iint_{s'_s} \mathcal{J} \cdot \mathbf{ds}' = \sigma \iint_{s'_s} \mathcal{E} \cdot \mathbf{ds}' \tag{2.1.8}$$

Substituting (2.1.7) and (2.1.8) into (2.1.6) and substituting Gauss' law for the charge enclosed gives:

$$I(z+\Delta z,t) - I(z,t) + \sigma \iint_{s'_s} \mathcal{E}_t \cdot \mathbf{ds}' = -\epsilon \frac{d}{dt} \iint_{s'_s} \mathcal{E}_t \cdot \mathbf{ds}' \tag{2.1.9}$$

A per-unit-length conductance can be defined as:

$$\sigma \lim_{\Delta z \to 0} \frac{1}{\Delta z} \iint_{s'_s} \mathcal{E}_t \cdot \mathbf{ds}' = gV(z,t) \tag{2.1.10}$$

And a per-unit-length capacitance defined as:

$$\epsilon \lim_{\Delta z \to 0} \frac{1}{\Delta z} \iint_{s'_s} \mathcal{E}_t \cdot \mathbf{ds}' = cV(z,t) \tag{2.1.11}$$

Rearranging (2.1.9), taking the limit as $\Delta z \to 0$, and then substituting (2.1.10) and (2.1.11) will give the second transmission line equation:

$$\frac{dI(z,t)}{dz} = -gV(z,t) - c\frac{dV(z,t)}{dt} \tag{2.1.12}$$

The telegrapher's equations, (2.1.5) and (2.1.12), can be written in phasor form by taking $\frac{d}{dt} \Leftrightarrow j\omega$:

$$\frac{dV(z)}{dz} = -(r + j\omega l)I(z) \tag{2.1.13}$$

$$\frac{dI(z)}{dz} = -(g + j\omega c)V(z) \tag{2.1.14}$$

These transmission line equations form the basis for calculating transmission line current and voltage models. Using the telegrapher's equations, the currents and voltages can be found everywhere on the line. Unfortunately, this simple solution has a big pitfall, it can't represent radiation along the transmission line structure. Section 2.2 will talk about methods used to represent radiation and present an overview of the derivation for the solution utilized in this study.

2.2 Transmission Line Radiation

The transmission line solution found in section 2.1 has no mechanism for representing radiation. There are many recent solutions that attempt to represent this radiation; such as

Modified Enhanced Transmission Line Theory[9], Transmission Line Super Theory[2], and some Method of Moments iterative solutions[1]. These methods similarly rederive the transmission line telegrapher's equation's using a complex Green's function. This produces a modified version of transmission line theory that contains complex per-unit-length parameters capable of representing radiation loss, unlike the classical transmission line model.

It's been shown previously that these existing models are unable to predict the high frequency emissions of typical transmission lines. Clayton Paul[7] showed that the model underpredicts the high frequency emissions of an electrically short transmisssion line circuit. Storer and King[11], West *et al.*[12], and Besnier *et al.*[6] have all obsereved the radiation mechanisms of a transmission line circuit may be dominated by the discontinuities at the line terminations rather than a continuous leakage along the line. In this section, we will repeat the derivation of the telegrapher equations and show another method to represent radiation from the transmssion line circuit.

2.2.1 Clayton R. Paul Representation

Clayton Paul[8, Chapter 11] has outlined an approach to represent radiaiton from the transmssion line cicuit that doesn't involve solving a complex Green's funciton. He rederives the transmission line equations with an incident electric field plane wave excitation. This derivation follows quite closely with the derivation from section 2.1, straying only slightly in the boundary condition definitions. This derivation produces the transmission line equations:

$$\frac{dV(z,t)}{dz} + rI(z,t) + l\frac{dI(z,t)}{dt} = \frac{d}{dt}\int_a^{a'} \mathcal{B}^{inc} \cdot \hat{\mathbf{n}} dl \tag{2.2.1}$$

$$\frac{dI(z,t)}{dz} + gV(z,t) + c\frac{dV(z,t)}{dt} = -g\int_a^{a'} \mathcal{E}^{inc} \cdot \mathbf{dl} - c\frac{d}{dt}\int_a^{a'} \mathcal{E}^{inc} \cdot \mathbf{dl} \tag{2.2.2}$$

We can substitute a per-unit-length distributed current and voltage source with the relation:

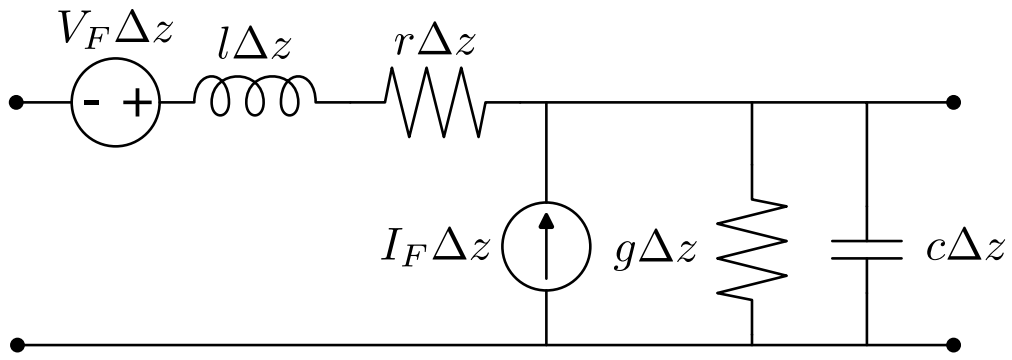

Figure 2: The per-unit-length equivalent circuit of a two conductor transmission line including the distributed radiation sources

$$V_F(z,t) = \frac{d}{dt}\int_a^{a'} \mathcal{B}^{inc}\cdot\hat{\mathbf{n}}dl \tag{2.2.3}$$

$$I_F(z,t) = -g\int_a^{a'} \mathcal{E}^{inc}\cdot\mathbf{dl} - c\frac{d}{dt}\int_a^{a'} \mathcal{E}^{inc}\cdot\mathbf{dl} \tag{2.2.4}$$

Then, writing these equations in phasor notation, we have:

$$\frac{dV(z)}{dz} + (r+j\omega l)I(z) = V_F(z) \tag{2.2.5}$$

$$\frac{dI(z)}{dz} + (g+j\omega c)V(z) = I_F(z) \tag{2.2.6}$$

A per-unit-length equivalent cirucit of this radiation model is shown in figure 2. This model has the same series inductance and resistance and the same shunt admittance and capcitance as before. Now, there is a series voltage source and a shunt current source that act to represent the susceptibility(or reciporically the emissions) from an incident plane wave.

This example used a simple two conductor transmission line. Paul[8, Chapter 12] has also extended these notions to multiconductor transmission lines. The developed multiconductor transmission line equations are straight forward to arrive at and have an identical form to the two conductor equations using a matrix notion.

2.3 Per-Unit-Length Parameters

The per-unit-length parameters of resistance, inductance, conductance, and capacitance are essential to solving for the currents and voltages from the telegrapher's equations. These quantities define the relationship between the field levels and circuit quantities on the transmission line. In this section, we will look at the formulation of the per-unit-length parameters for a two conductor transmission line.

As Paul outlines in [8, chapter 1], the per-unit-length parameter relationships in (2.3.1) and (2.3.3) are derived from the transmission line equations.

$$lc = \mu\epsilon \tag{2.3.1}$$

$$gl = \sigma\mu \tag{2.3.2}$$

$$\frac{g}{c} = \frac{\sigma}{\epsilon} \tag{2.3.3}$$

2.3.1 Inductance

The current loop formed by current flowing down the top conductor and returning on the lower conductor will have a per-unit-length inductance, l associated with it. The relationship in equation (2.3.1) forms the basis for solving an arbitrary cable cross-section for this per-unit-length inductance. Given a lossless medium homogeneous in ϵ and μ, per-unit-length inductance can be obtained from:

$$l = \mu\epsilon c^{-1} \tag{2.3.4}$$

2.3.2 Conductance

There is a transverse conduction current directed towards the ground conductor. This effect can be represented in a length of line by a per-unit-length conductance, g, between the conductors. From (2.3.3), we can also solve for per-unit-length conductance in a lossy medium,

homogeneous in σ, as:

$$g = \frac{\sigma}{\epsilon} c \tag{2.3.5}$$

Equation (2.3.5) represents the resistive losses in the dielectric medium using a finite conductivity σ. This proves insufficient as the losses in the dielectric are typically dominated by the polarization loss.

When an electric field is applied to a dielectric, dipoles form and attempt to align with the applied field. As the frequency of the electric field increases, the dipoles begin to increasingly lag behind the quickly changing field direction, creating loss in the material. This polarization loss is represented by a frequency dependent complex permittivity in the dielectric material:

$$\epsilon_l = \epsilon - j\epsilon_p \tag{2.3.6}$$

Applying this to Ampere's law produces a new effective conductivity:

$$\sigma_{eff} = \sigma + \omega\epsilon_p = \omega\epsilon \tan\delta \tag{2.3.7}$$

This new effective conductivity can be applied to (2.3.3) to find the per-unit-length conductance incorporating polarization losses as:

$$g = \frac{\sigma_{eff}}{\epsilon} c = \omega \tan\delta c \tag{2.3.8}$$

2.3.3 Capacitance

Similarly to the conduction current, there is a displacement current between the lines that can be represented by a per-unit-length capacitance, c. From the formulation of inductance and conductance, it's obvious that with a quality solution for capacitace, these other quantities are straight forward to calculate. For a few simple structures, there are analytic solutions

for the capacitance. Unforunately, these solutions do not easily extend to even mildly complex cable structures. For this, we need to use a neumarical solution to approximate the capacitance. This neumerical approach will be further explored in Chapter III.

Solving the assembly with no dielectric in place produces a real capacitance result that can easily be solved for inductance.

$$l = \mu\epsilon c_0^{-1} \tag{2.3.9}$$

Applying a complex permativity, as in equation (2.3.6), to the numerical calculation will produce a complex capacitance that has the cable losses incorperated:

$$c_L = c_R + jc_I \tag{2.3.10}$$

From this, the per-unit-length capacitance and conductance come out as:

$$c = c_R \tag{2.3.11}$$

$$g = -\omega c_I \tag{2.3.12}$$

2.3.4 Resistance

Ohmic losses along the line due to a finite conductance can be represented as a per-unit-length resistance, r. Solving for this per-unit-length resistance can be a very simple problem. It can be approximated with surprising accuracy by modifying the familiar skin depth equation to:

$$r = \frac{1}{2\pi r_w \sigma\delta} = \frac{1}{2r_w}\sqrt{\frac{f\mu}{\pi\sigma}}\ \left(\frac{\Omega}{m}\right) \tag{2.3.13}$$

Where r_w is the wire radius.

As Paul notes in [8, chapter 4], for this per-unit-length resistnace solution, the currents have been assumed to be symmetric about the center of the conductor cross-section. This tends to be a good approximation for normal transmission line assemblies operating at the

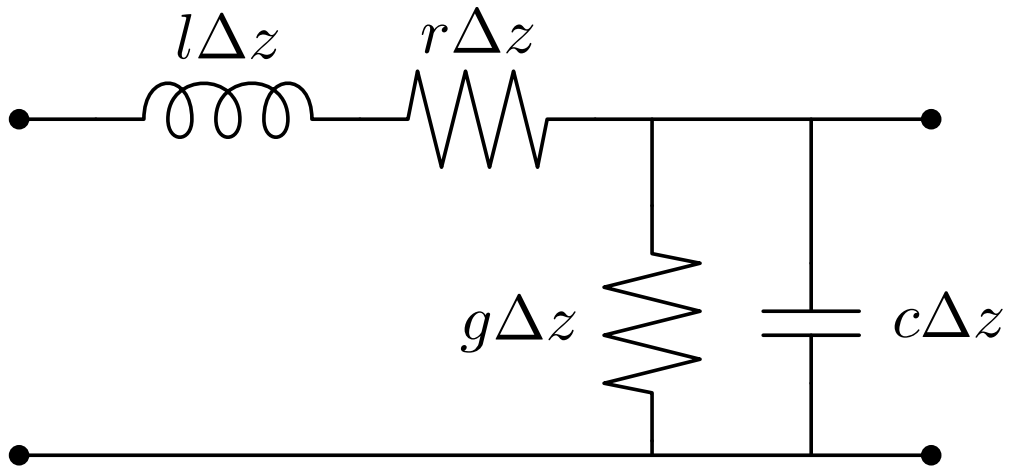

Figure 3: The per-unit-length equivalent circuit of a two conductor transmission line

frequencies discussed in this paper. More notably, finding a more accurate solution proves to be a difficult task for minimal improvment. For the purposes of this simulation work, the ohmic losses are significantly less than radiated losses.

2.3.5 Per-Unit-Length Equivalent Circuit

Taking these four circuit quantities, a per-unit-length equivalent circuit diagram can be made to show a more intuitive view of the relationship described by the transmission line equations. Figure 3 shows this diagram for the two conductor line, same as figure 1. the per-unit-length inductance and resistance act as series elements, and the per-unit-length capacitance and conductance act as shunt elements distributed along the length of the line.

CHAPTER III

Simulation Work

For complex transmission line structures, there are few analytic models for calculating the per-unit-length parameters. Instead, a numerical approach is commonly used to approximate the capacitance, inductance, and conductance. This study uses a finite element analysis tool, FreeFEM++[4], to calculate these parameters. These per-unit-length parameters are then used in the analysis of Clayton Paul's multiconductor transmission line model[8]. This model was written in c++ by my advisor, Dr. James West.

These are the two key pieces of software used for all the simulations in this study. This paper does not go over the transmission line model in great detail, for more information on it, see [8]. This chapter will outline the per-unit-length parameter solver implementation in FreeFEM++ and also validate this finite element method against some analytic models.

3.1 A Per-Unit-Length Solver

To implement an arbitrary per-unit-length solver, FreeFEM++[4] has been used. FreeFEM++ is an open source and efficient implementation of the finite element method. This allows me to utilize this package in the overall software suite being built. The initial goal is to have the ability to calculate the per-unit-length capacitance of an arbitrary transmission line structure. This solution will then be extended to solving for all the per-unit-length parameters as discussed in section 2.1. To illustrate the use of FreeFEM++ and the finite element method to solve for capacitance, a simple two conductor transmission line, shown in figure 4, will again be used. This capacitance solution will be used to calculate the inductance and

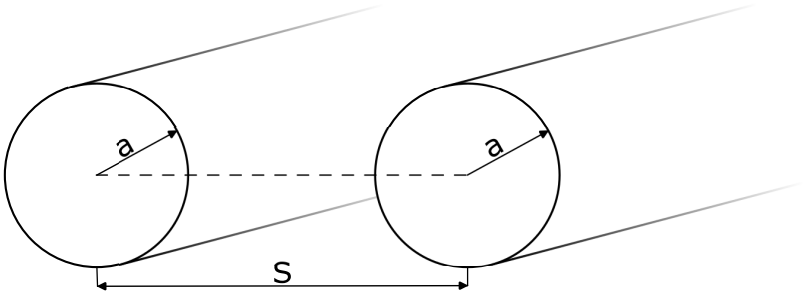

Figure 4: Straight two wire transmission line structure for FEM demonstration

conductance, and the two conductor model will be used to define a solution for arbitrary multiconductor transmission lines.

3.1.1 Meshing the Structure

Start in FreeFEM++ by meshing the cross-sectional structure of our transmission line. While FreeFEM++ can import mesh files directly, it has an advanced automatic mesh generator built in that is straightforward to use. For this mesh generation tool, all the conductors and meshing domain boundaries are defined by parameterized curves as borders in the software. Then, the number of mesh points along each border must also be defined. Creating a finer mesh can often help to improve the calculation accuracy, but if the mesh is too fine, there will be instability in the simulation and the accuracy will suffer. I have found that adding ten mesh points per unit arc length of the border provides a good middle of the road between accuracy, stability, and computation time. This means, for a circular conductor with radius 1 unit, approximately 60 mesh points should be sufficient in providing an accurate calculation. The mesh created by FreeFEM++ when fed these parameters for the twin-lead example structure is shown in figure 5.

There are a couple of things that can be done while meshing to provide a more accurate final result. Adding a small radius to any hard corners, like at the sides of a ground plane, can help to smooth out the mesh and avoid instability, as seen in figure 6. When building an 'infinite' ground plane, making it 20 times wider than the farthest conductor will provide

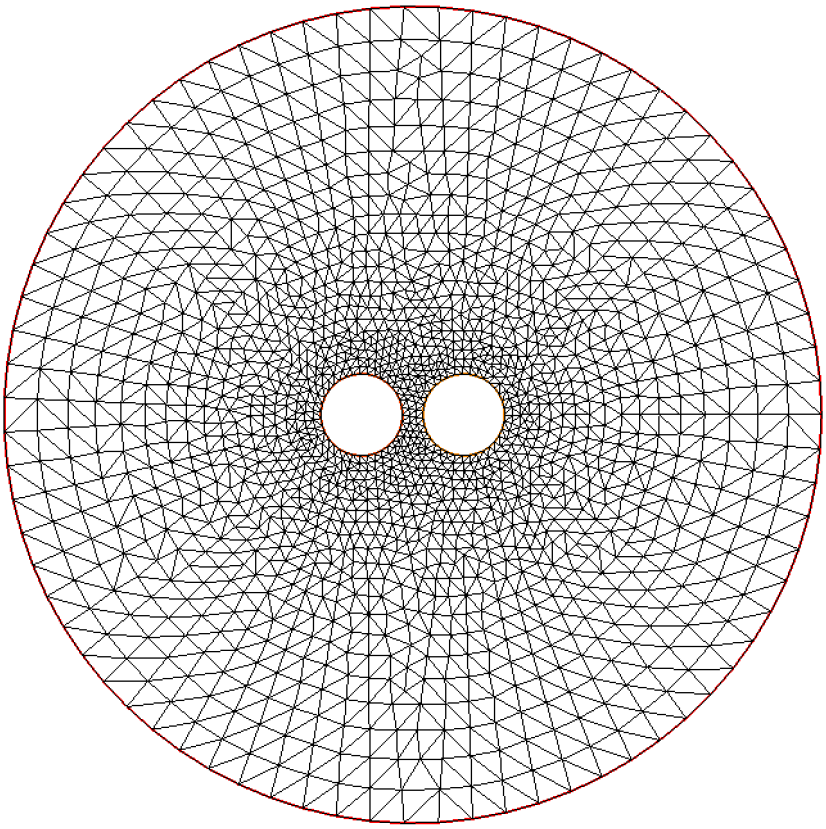

Figure 5: Mesh created by FreeFEM++ for a two conductor transmission line cross-section

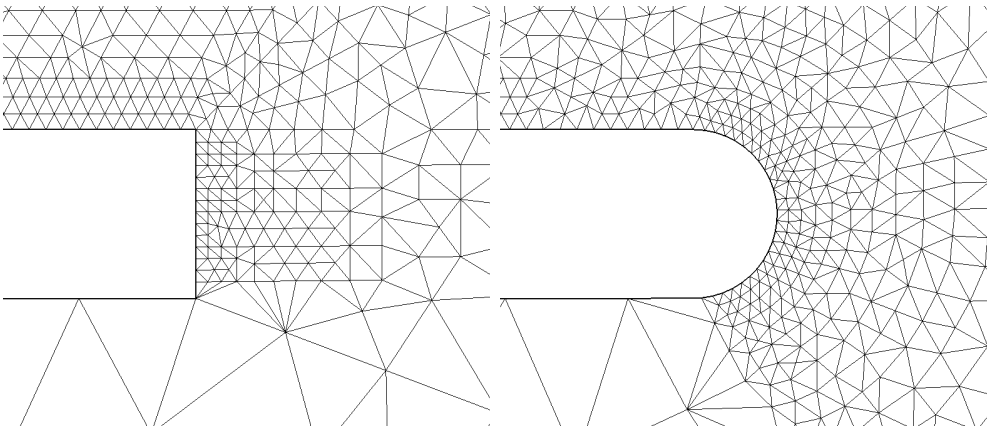

Figure 6: Mesh comparison between hard corner and rounded corner

a satisfactory approximation while minimizing computation time. Most transmission line structures will be on the order of a centimeter. By operating in these units, rather than meters, within FreeFEM++, the mesh will be produced more cleanly and rounding errors will be negligible. When producing a domain boundary for an unbounded cross-section, the number of mesh points can be far coarser than on the conductors because the electrostatic potential should decay to zero at this border. Also, moving the domain boundary of an unbounded problem father from the conductors of interest will improve the result. At some distance, there will be diminishing returns for a more involved computation. I've found that meshing the ground plane three times wider than the farthest conductor is sufficient to not interfere with the solution.

3.1.2 Solving Poisson's Equation

Once the structure has been meshed, the boundary conditions need to be defined and Poisson's equation needs to be solved to obtain the electrostatic potential everywhere in the cross-sectional domain. This is necessary to calculate the per-unit-length capacitance.

Start by writing out Poisson's equation in its classical form

$$\begin{cases} -\nabla^2 u = \dfrac{\rho}{\epsilon} & \text{in } \Omega \\ \\ u = u_d & \text{on } \delta\Omega \end{cases} \tag{3.1.1}$$

Defining u as the unknown electrostatic potential, ρ the source term space charge density, ϵ the permittivity, Ω the unit disk, and $\delta\Omega$ the boundary of the unit disk.

Multiplying Poisson's equation by a test function v

$$-\int_\Omega \left(\epsilon\,\nabla^2 u\right) v\ ds = \int_\Omega \rho v\ ds \tag{3.1.2}$$

Integrating by parts

$$-\int_\Omega \left(\epsilon\,\nabla^2 u\right) v\ ds = \int_\Omega \epsilon\,\nabla u \cdot \nabla v\ ds - \int_{\delta\Omega} \epsilon\,\frac{\delta u}{\delta n} v\ dl \tag{3.1.3}$$

The test function v vanishes on the parts of the boundary where u is known. For the problems solved in this study, that is all the boundaries. This presents as the following limit

$$\int_{\delta\Omega} \epsilon \frac{\delta u}{\delta n} v\ dl \longrightarrow 0 \tag{3.1.4}$$

Plugging (3.1.4) back into equation (3.1.2)

$$\int_\Omega \epsilon\,\nabla u \cdot \nabla v\ ds = \int_\Omega \rho v\ ds \tag{3.1.5}$$

There are no free charges in this problem, meaning $\rho = 0$ and $\int_\Omega \rho v\ ds = 0$. This gives Poisson's equation in its variational form which is used in FreeFEM++

$$\int_\Omega \epsilon \nabla u \cdot \nabla v\ ds + \text{Dirichlet Boundary Conditions} = 0 \tag{3.1.6}$$

The Dirichlet boundary conditions are quite straight forward to define. A test voltage, V, is applied to one conductor and the other conductor is driven to 0. Also, for this unbounded structure, the boundary of the domain is left floating. If this boundary were placed at infinity, it would be acceptable to apply a boundary condition of 0 to it.

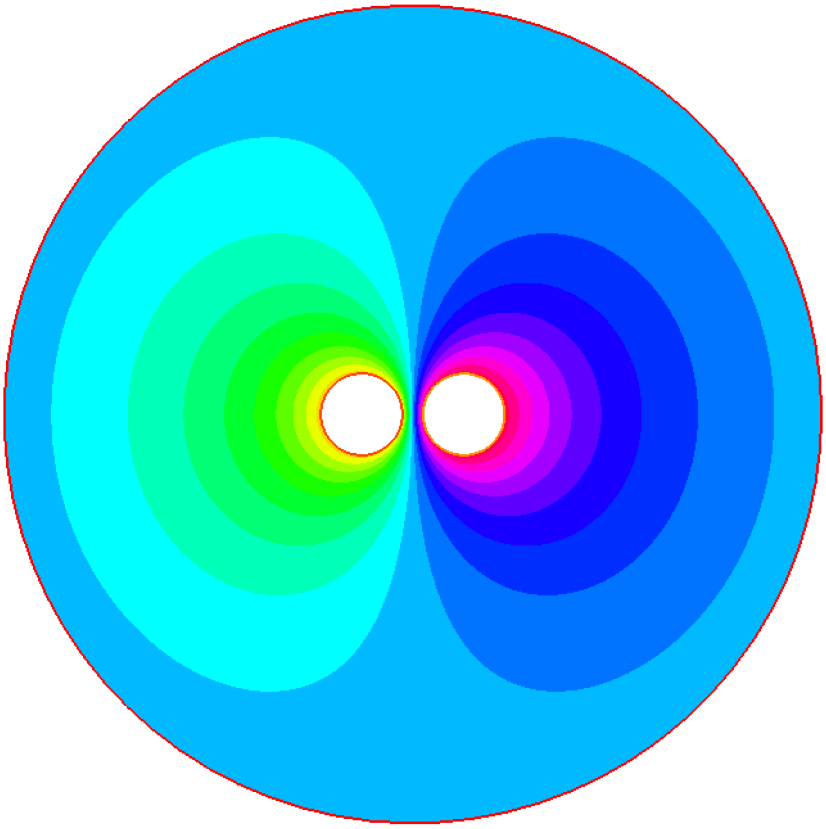

Figure 7: The electrostatic potential everywhere in the meshed domain

Plugging this variational equation along with the boundary conditions into FreeFEM++ is straightforward. FreeFEM++ will take the material properties from ϵ, and use the specified basis function to solve for the lowest energy equilibrium solution. This will produce a mesh containing the electrostatic potential, u, everywhere in the domain, as shown in figure 7.

3.1.3 Calculating the Capacitance

We now have a mesh with the electrostatic potential at each point. To calculate the capacitance from this is straightforward.

From Gauss's law and the divergence theorem, we can calculate the total charge enclosed by a conductor as

$$Q = \int_{\Omega} \epsilon(\nabla \cdot \mathbf{E}) ds \tag{3.1.7}$$

$$= \oint_{\delta\Omega} \epsilon(\hat{\mathbf{n}} \cdot \mathbf{E}) dl \tag{3.1.8}$$

$$= -\oint_{\delta\Omega} \epsilon(\hat{\mathbf{n}} \cdot \nabla u) dl \tag{3.1.9}$$

This integral must be numerically calculated from the mesh of electrostatic potential calculated previously using Poisson's equation. Taking the gradient of this mesh and integrating over the boundary of the conductor of interest will provide the total charge on that conductor. Finally, combining this with the test voltage applied in the boundary condition we get the desired per-unit-length capacitance:

$$C = -\frac{1}{V} \int_{\delta\Omega} \epsilon[\hat{\mathbf{n}} \cdot \nabla u] dl \tag{3.1.10}$$

3.1.4 Remaining Per-Unit-Length Parameters

Section 2.1 talks about how to extend a capacitance solver to be able to calculate for the other per-unit-length parameters. In this section, we will outline exactly how to do that in FreeFEM++.

For a transmission line with lossy insulators, we need only alter the permittivity in equations (3.1.6) and (3.1.10) to represent losses in the dielectric material. In FreeFEM++ this is done right after defining the mesh. A complex piecewise permittivity can be defined attributing a different constant to the region containing insulators. A mesh of this is shown in figure 8.

The calculated capacitance will be a complex value, $c_L = c_R + jc_I$, and the capacitance and conductance can be calculated as

$$c = c_R \tag{3.1.11}$$

$$g = -\omega c_I \tag{3.1.12}$$

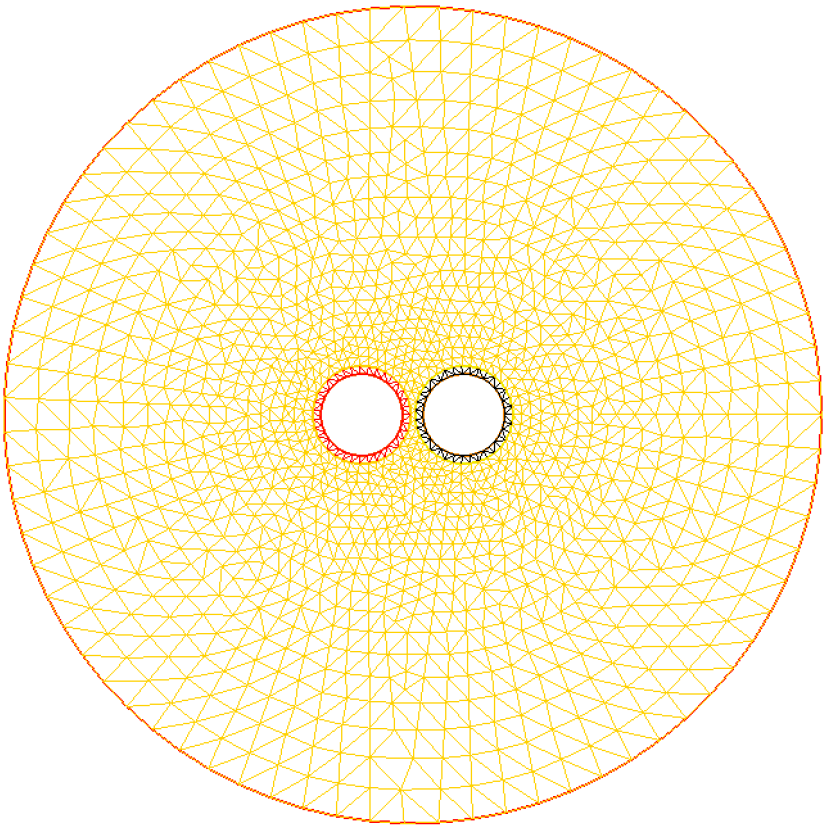

Figure 8: Mesh created by FreeFEM++ for a two conductor transmission line with insulators

To calculate the inductance, you must remesh the structure without the dielectric in place. The solution will be a real capacitance, c_0. The inductance can be calculated as

$$l = \mu_0 \epsilon_0 c_0^{-1} \tag{3.1.13}$$

3.1.5 Multiconductor transmission lines

Extending this solution from a two conductor line to a multiconductor transmission line is straightforward. As outlined in by Paul[8] we must expand the capacitance out to a matrix that represents the displacement current flowing between the ith and jth conductors in the transverse plane. The diagonal of this matrix, c_{ii}, represents the total displacement current flowing from the ith conductor to ground in the transverse plane.

$$\mathbf{C} = \begin{bmatrix} c_{11} & c_{12} & \cdots & c_{1n} \\ c_{21} & c_{22} & \cdots & c_{2n} \\ \vdots & \vdots & \ddots & \vdots \\ c_{n1} & c_{n2} & \cdots & c_{nn} \end{bmatrix} \tag{3.1.14}$$

Because of the reciprocity of transmission line structures, we can use symmetry to reduce the number of calculations needed to fill the matrix

$$\mathbf{C} = \begin{bmatrix} c_{11} & c_{12} & \cdots & c_{1n} \\ c_{12} & c_{22} & \cdots & c_{2n} \\ \vdots & \vdots & \ddots & \vdots \\ c_{1n} & c_{2n} & \cdots & c_{nn} \end{bmatrix} \tag{3.1.15}$$

This matrix can be interpreted similarly to an s-parameter matrix. Giving the matrix entries as follows

$$c_{ij} = \frac{Q_i}{V_j} \tag{3.1.16}$$

Drive conductor j with a test voltage, V, and set all other conductors to a voltage of zero. Then, use the finite element solution to calculate the charge, Q, on conductor i. Repeat this procedure to fill the entire matrix.

From here, it extends to the other per-unit-length parameters in an identical manner as before. The problem must first be meshed and solved with no dielectric material in place. This will produce a real capacitance matrix, $\mathbf{C}_0$, which can solve for an inductance matrix as

$$\mathbf{L} = \mu_0 \epsilon_0 \mathbf{C}_0^{-1} \tag{3.1.17}$$

Then, remesh the domain while incorporating the lossy dielectric as a complex permittivity and solve again for the capacitance matrix. This will produce a complex capacitance matrix

$$\mathbf{C}_L = \mathbf{C}_R + j\mathbf{C}_I = \begin{bmatrix} c_{11} + jc_{11} & c_{12} + jc_{12} & \cdots & c_{1n} + jc_{1n} \\ c_{12} + jc_{12} & c_{22} + jc_{22} & \cdots & c_{2n} + jc_{2n} \\ \vdots & \vdots & \ddots & \vdots \\ c_{1n} + jc_{1n} & c_{2n} + jc_{2n} & \cdots & c_{nn} + jc_{nn} \end{bmatrix} \tag{3.1.18}$$

Again, calculating the capacitance and conductance matrix follows similarly.

$$\mathbf{C} = \mathbf{C}_R \tag{3.1.19}$$

$$\mathbf{G} = -\omega \mathbf{C}_I \tag{3.1.20}$$

3.2 Validation of the Capacitance Solver

Now that the capacitance solver has been implemented, it's important to be validated to ensure it's an accurate solution. In this section, a couple simple transmission lines, with analytic models, will be tested in the FreeFEM++ software to ensure proper calculation of the capacitance values.

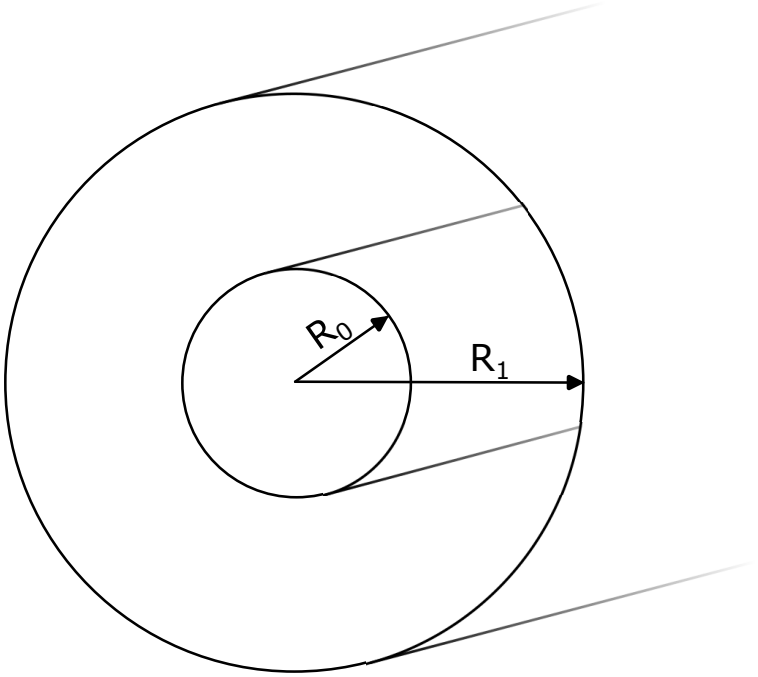

Figure 9: Coaxial line cross-section for finite element analysis

3.2.1 Coaxial Transmission Line

The first transmission line structure to be tested is a coaxial transmission line. This presents possibly the simplest testable case. It has a bounded mesh domain, with smooth edges, and defined boundary conditions. A diagram of this cross-section can be seen in figure 9 and the coinciding mesh in figure 10.

The coaxial cross-section was modeled in the finite element tool and the capacitance results are shown in figure 11 being compared to the analytic solution for a coaxial line from (3.2.1). The finite element analysis results are very accurate, having a maximum error, when compared to the analytic solution, of 0.40% at a ratio of 2 and quickly dropping to an error of 0.10% as R_1 increases.

$$c = \frac{2\pi\epsilon_0\epsilon_r}{ln\left(\frac{R_1}{R_0}\right)} \tag{3.2.1}$$

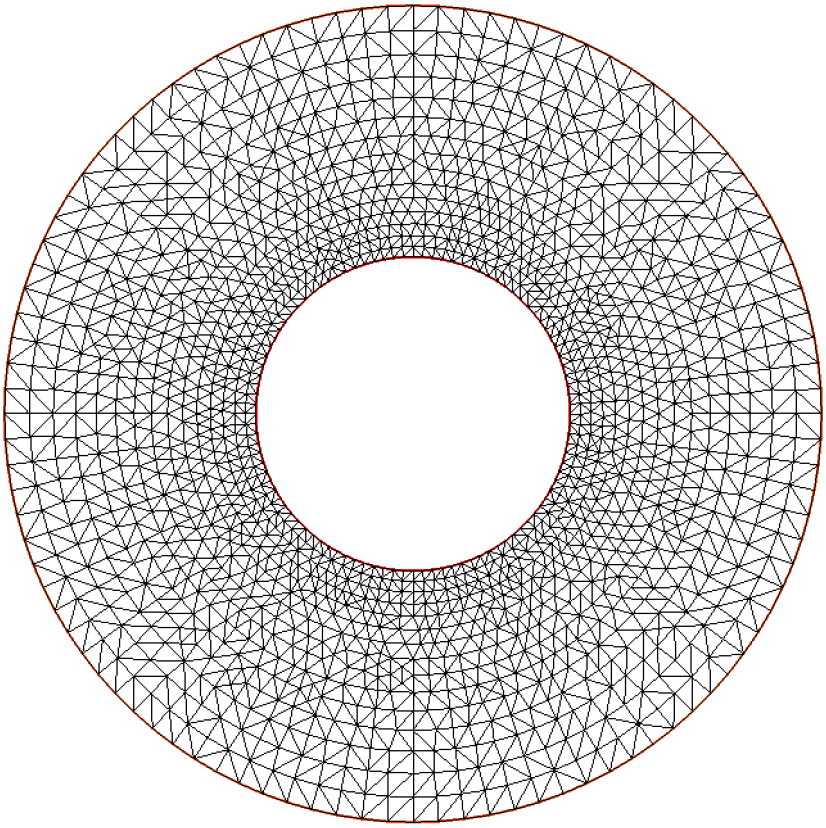

Figure 10: Coaxial line mesh from FreeFEM++

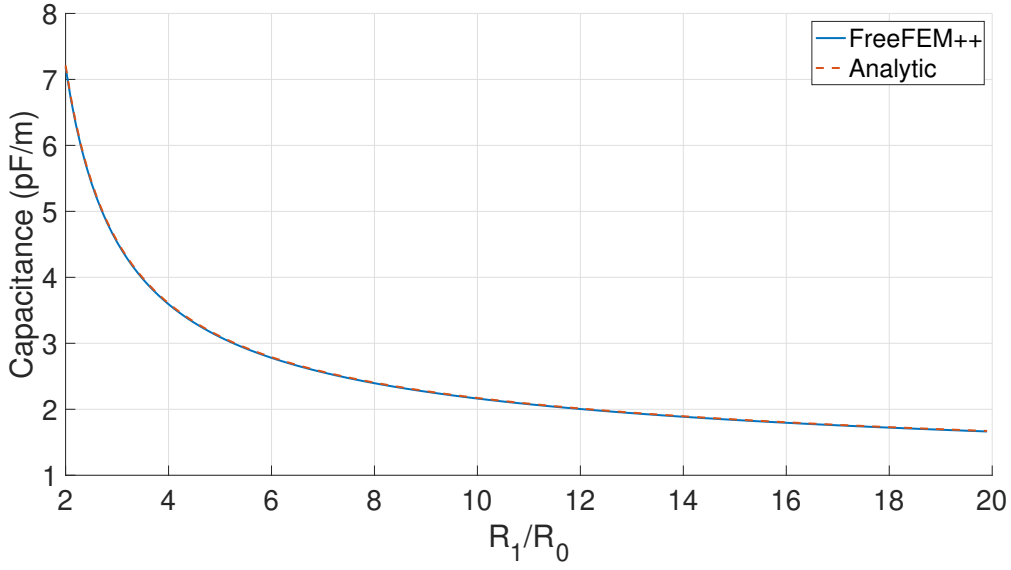

Figure 11: Coaxial line capacitance vs conductor radius ratio.

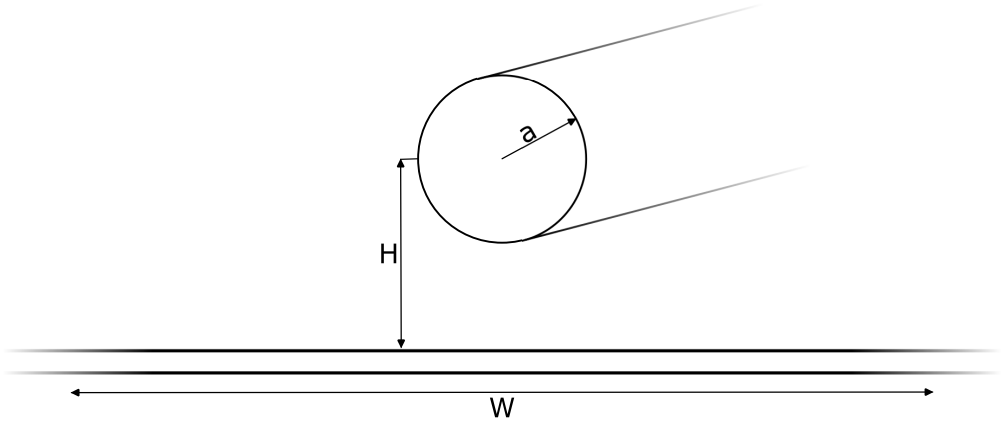

Figure 12: Single conductor over a ground plane cross-section for finite element analysis

3.2.2 Single Conductor over a Ground Plane

The next structure to be tested is a single conductor over an 'infinite' ground plane. This is a good next step; it has an unbounded domain and a rectangular conductor for the ground plane. It has the added benefit of providing some insight into the width needed to approximate an infinite ground plane. A diagram of this structure is shown in figure 12.

Figure 13 shows the capacitance calculated from FreeFEM++ as the width of the ground plane increases. This figure compares it to the analytic solution for a single wire over a ground plane, from equation (3.2.2). With a width of only twice the height, there is an error of 27.6% when compared to the analytic solution. This error decreases quickly to 0.5% at a $\frac{W}{H}$ ratio of 15. From this, we can gleam that having the ground plane 15-20 times wider than the farthest conductor provides a quality approximation to an infinite ground plane.

$$c = \frac{2\pi\epsilon_0\epsilon_r}{cosh^{-1}\left(\frac{H}{a}\right)} \tag{3.2.2}$$

3.2.3 Twin-Lead Over a Ground Plane

For the final test case to validate the capacitance solver, a twin-lead transmission line over a ground plane was analyzed. This test case again adds difficulty onto the previous problem;

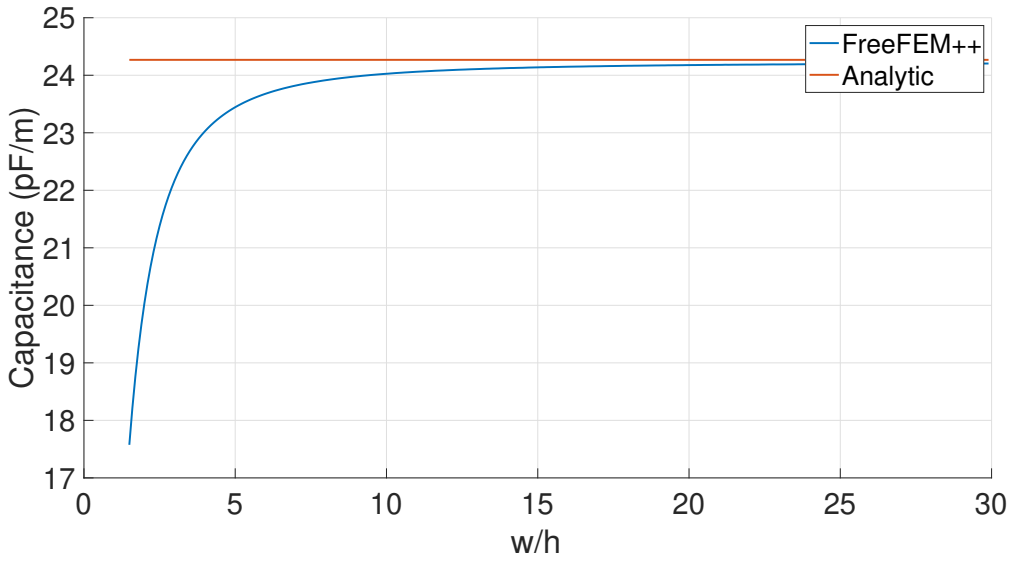

Figure 13: Single conductor over a ground plane capacitance vs width of ground plane.

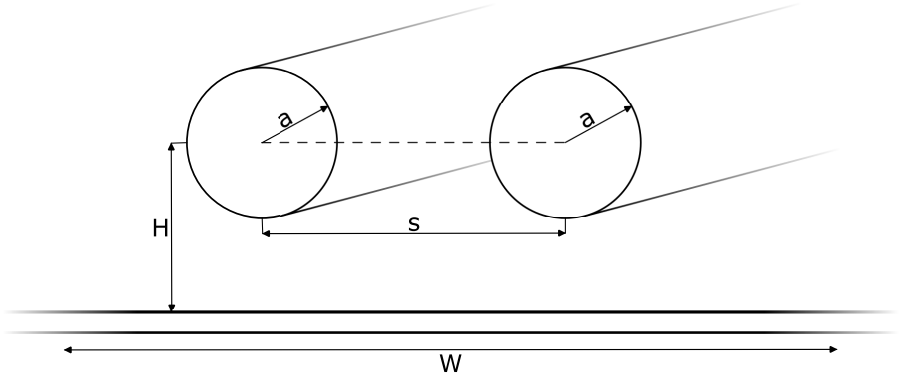

Figure 14: Twin-lead line over a ground plane cross-section for FEM analysis

there is an unbounded mesh, a rectangular ground plane, and a third conductor that requires a boundary condition. Figure 14 shows a diagram of the situation being modeled.

Handling the domain boundary is straightforward. It needs to be sufficiently far from any conductor of interest and can be left as a floating boundary. The results of the finite element analysis are shown in figure 15. They are being compared to the analytic result for a twin-lead transmission line without a ground plane, from equation (3.2.3). When the line is close to the ground plane, it has a significant contribution to the overall capacitance and the compared results do not match well. As the height to the ground plane increases, and

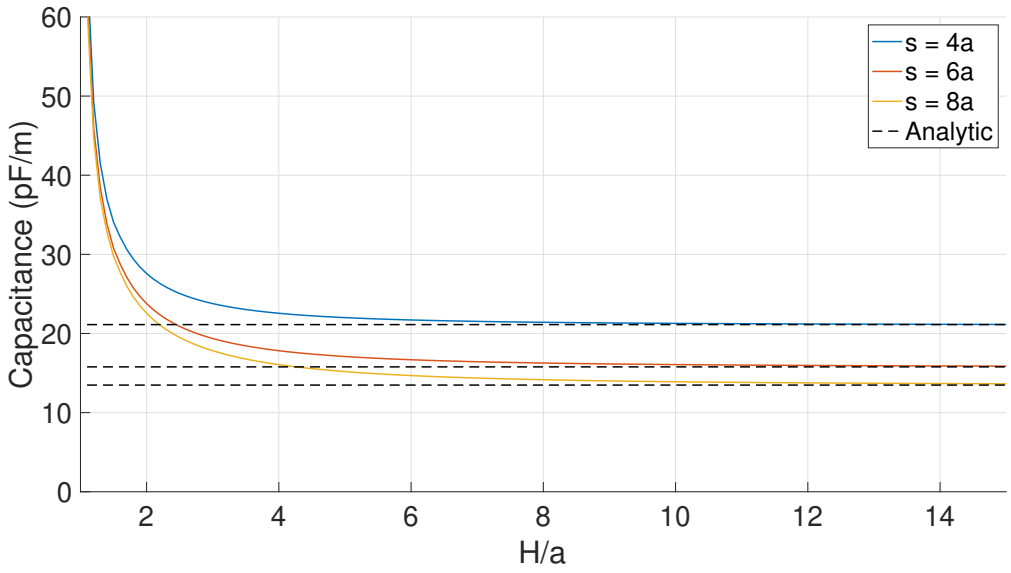

Figure 15: Twin-lead over a ground plane capacitance vs height above ground plane.

the interaction between the conductors and ground plane decreases, the numerical solution should converge to the referenced analytic solution for a twin-lead line. This again helps to build confidence that the transmission line solver is accurately calculating the capacitance of the transmission line structure.

$$c = \frac{2\pi\epsilon_0\epsilon_r}{cosh^{-1}\left(\frac{S-2a^2}{2a^2}\right)} \tag{3.2.3}$$

This test completes the focused FEM validation testing. In chapter IV, some experimental measurements are used to compare against the modeling software to further validate the per-unit-length calculation as well as the Paul transmission line model implemented by my advisor.

CHAPTER IV

Experimental Work

There are two parts to the experimental efforts of this project. The first was conducted in an anechoic chamber. The scattering parameters of a couple transmission line structures were measured to validate both the capacitance solver and the transmission line model implemented. The second part of the experimental effort took place in reverberation chambers. Here, the radiation characteristics of transmission lines were explored to try and determine the radiating mechanism of a practical transmission line circuit. In this chapter, we will go over the setup and results of these experiments. For all experimental test configurations, the lines were soldered to SMA bulkhead connectors, shown in figure 16. The transmission line was then stretched between either reverberation chamber walls or two aluminum plates, depending on the exact test configuration.

4.1 Anechoic Chamber

The anechoic chamber tests were conducted in an ETS-Lindgren fully anechoic chamber. This chamber was commercially produced by ETS-Lindgren and has been validated for operation down to 80 MHz. For these tests, the anechoic chamber was used as a quiet room rather than a direct field environment.

The experiments conducted serve as a crucial step towards validating the finite element method and transmission line model software packages. For the referenced simulation results during this validation testing, the conductors were assumed to be perfectly conducting, and the radiation from the wires was disregarded. This allowed for a more simple model, making

Figure 16: SMA bulkhead connectors used for measurement.

it easier to debug any errors. By employing this simplified model, it becomes easier to detect and troubleshoot any errors, improving the accuracy and reliability of the software.

A structure similar to that in [9] and [6], shown in figure 17, was used for these experiments. It contained a large aluminum ground plane, 100 cm by 60 cm, and two aluminum end plates, 60 cm by 60 cm. The structure was open on all other sides. Holes were drilled in the end plates to accommodate SMA bulkhead connectors, acting as wall penetrations. 14-guage uninsulated steel wire was stretched between the connectors to act as the transmission line. The two connectors not being driven by the VNA were terminated at the end plates with 50 Ω loads. To test, the structure was placed into the anechoic chamber and the scattering parameters were measured with a 2-port VNA.

Twin-lead Transmission Line

The first measurement configuration examined is shown in figure 18. It's a twin-lead transmission line over a ground plane with a ground plane height of 10 cm. The structure was

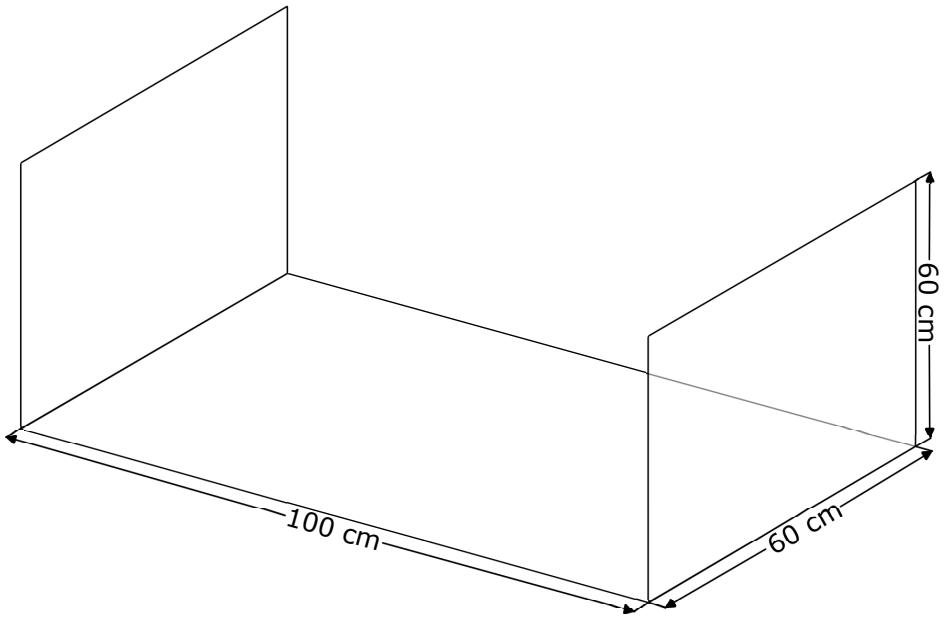

Figure 17: Aluminum structure supporting transmission line. 100x60 cm ground plane with 60x60 cm end plates.

measured using a 2-port VNA. Two ports were being driven while the other two ports were terminated in 50 Ω loads. This meant, for the full four port data, 6 measurements were conducted.

This structure represents one of the simplest cases possible to test the transmission line model code implemented in this work; assuming a wide spacing approximation, there is an analytic model to compare the capacitance values against and the transmission line structure is quite simple, leaving the transmission line code easy to track.

The results from the scattering parameter measurements can be seen in figures 19, 20, 21, and 22. From this we can see quite good agreement between the measured results in the anechoic chamber and the calculated results from the finite element method and transmission line model. There does appear to be a frequency offset, easily viewable at the peaks and nulls. This is due to a discrepancy in the length of the line between the model and the physical configuration. Adding a small length to the model in the code is able to remove this offset. There is also a decay present in the transmission coefficient measurements, in figure

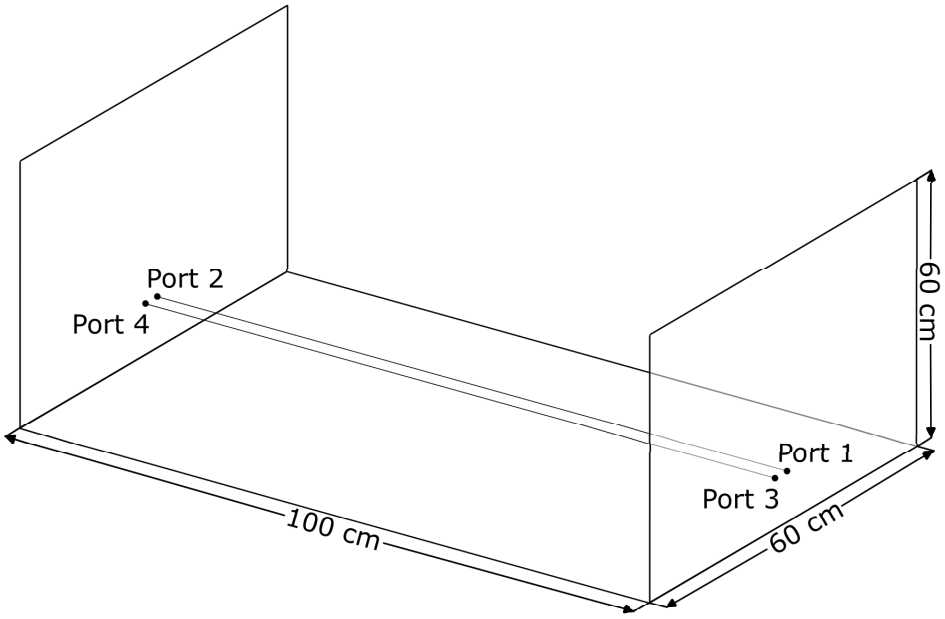

Figure 18: Twin-lead test setup. There is a 10 cm height above the ground plane and a 1 cm conductor spacing.

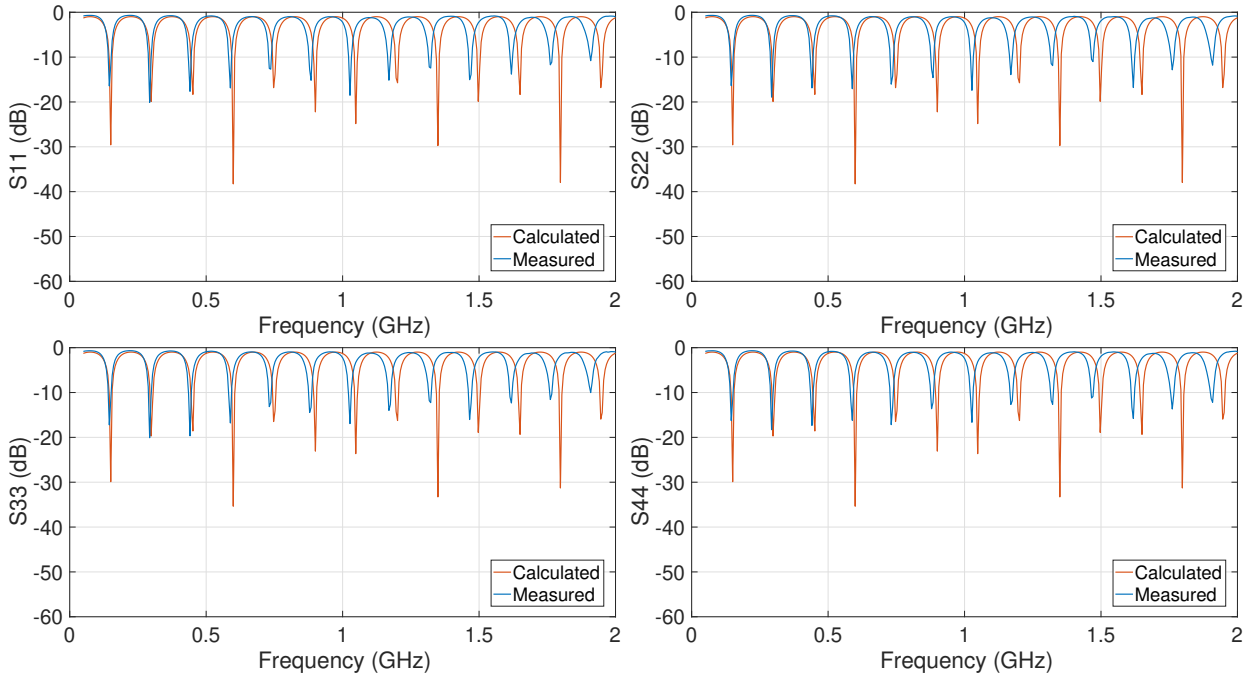

Figure 19: Reflection coefficients for twin-lead configuration

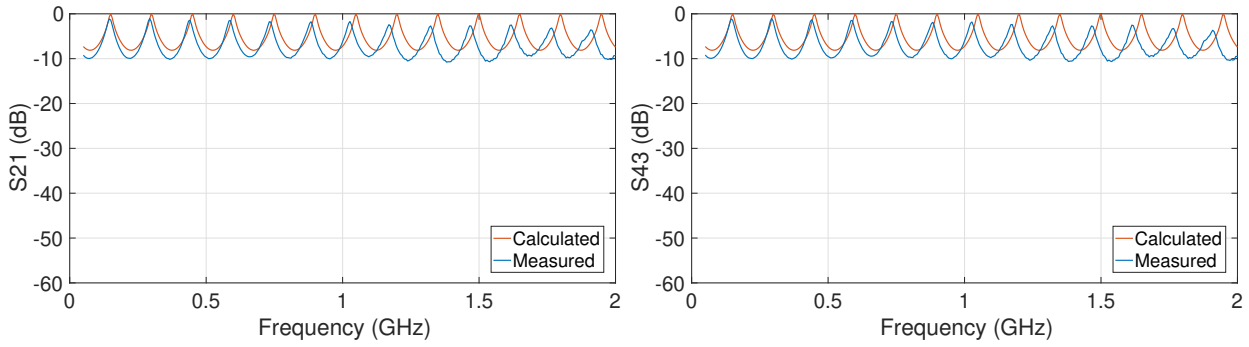

Figure 20: Transmission coefficients for twin-lead configuration

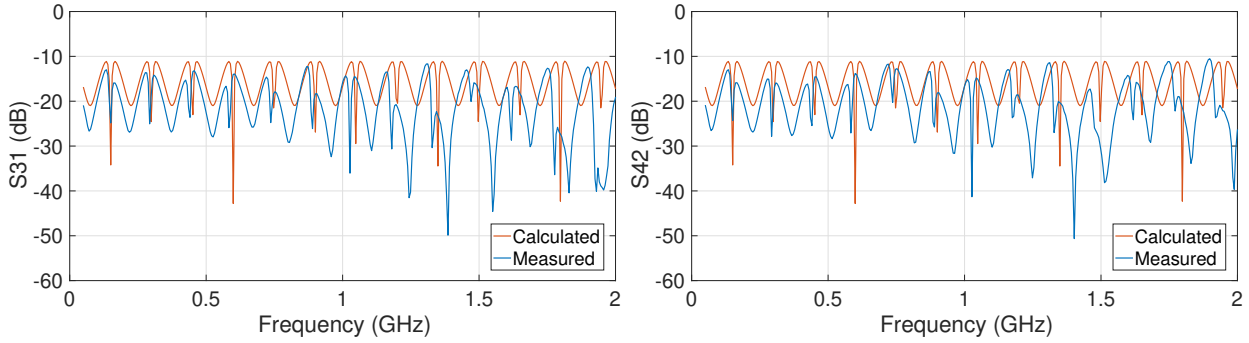

Figure 21: Near-End Cross Talk for twin-lead configuration

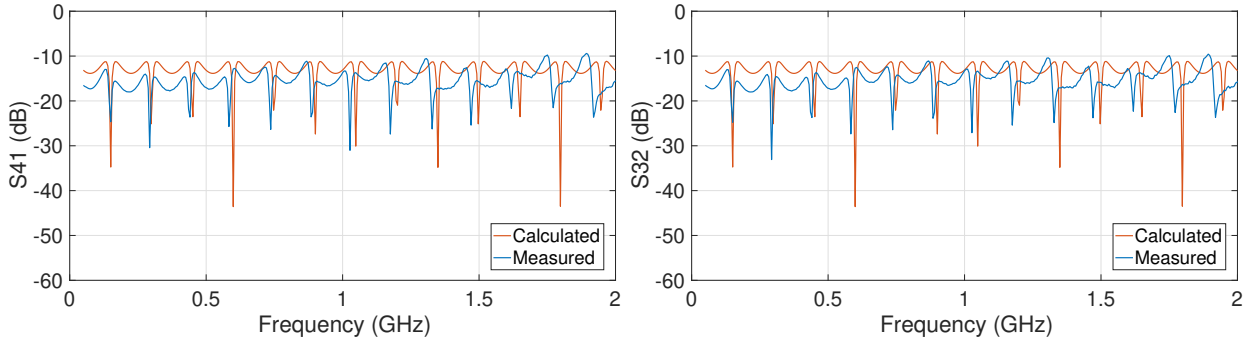

Figure 22: Far-End Cross Talk for twin-lead configuration

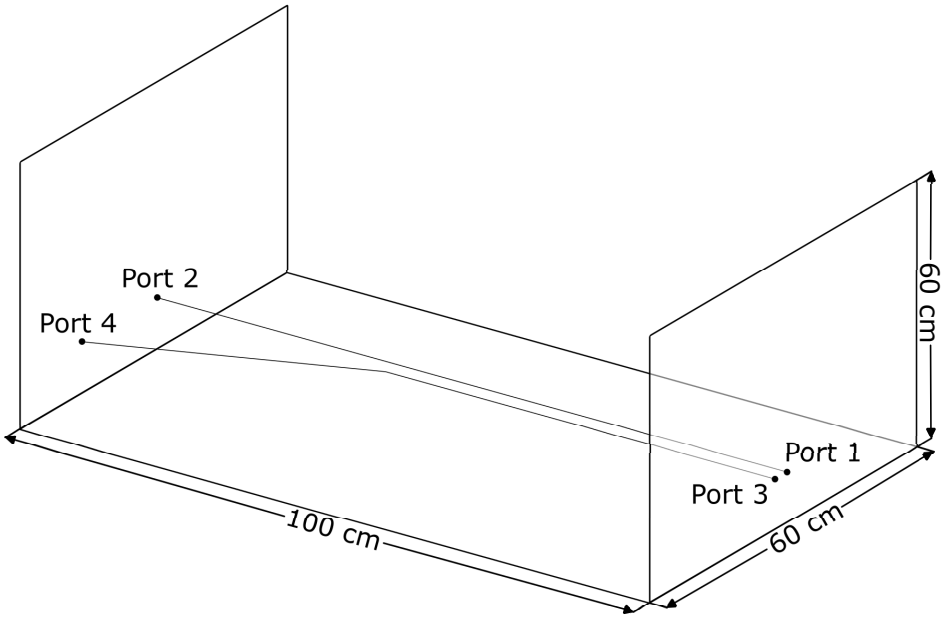

Figure 23: Branched line test setup. There is a 10 cm height above the ground plane. There is a 1 cm spacing in the twin-lead section and a 16 cm spacing at the widest point.

20, that isn't present in the simulated result. This is from the ohmic and radiated losses on the line that have been neglected in the simulation. These results provide confidence that the simulation model, per-unit-length calculation and transmission line model, is working properly.

Branched Transmission Line

The next measurement structure was a branched transmission line over a ground plane, as shown in figure 23. The twin-lead section has a 1 cm spacing and a length of 70 cm. The branch section has a length of 30 cm and an angle of 28°, giving a final connector spacing of 16 cm. Again, the connectors and conductors are 10 cm above the ground plane. Two ports were being measured while the other two ports were terminated in 50 Ω loads.

This structure presents a few challenges not present in the previous test that makes it a good next step in the validation process. The structure is modeled as three independent transmission lines, two single conductor lines over a ground plane and one twin-lead line

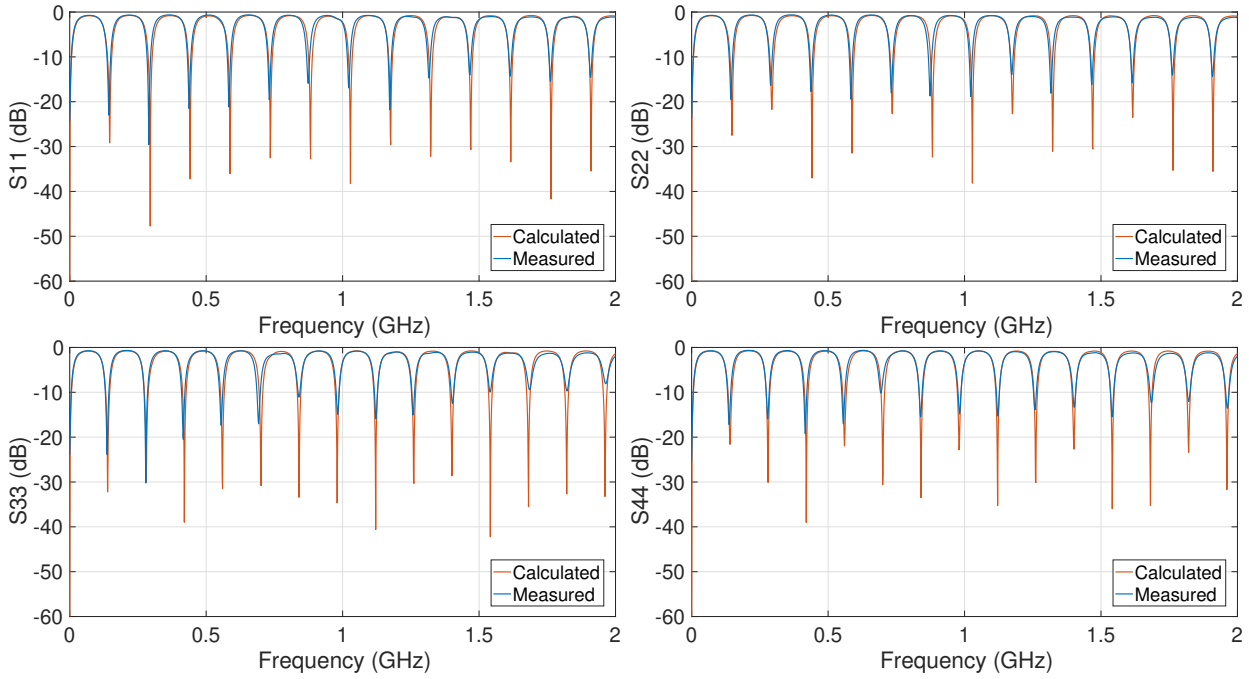

Figure 24: Reflection coefficients for branched line configuration

over a ground plane line. All of these have analytic models for the capacitance, allowing for more checking that the finite element method calculation is working properly. Having three independent lines also allows for a more strenuous test of the transmission line model.

The results for the branched line measurement are shown in figures 24, 25, 26, and 27. The measured scattering parameters match the simulated scattering parameters very well. The peaks and nulls line up well in the reflection and transmission coefficients, figures 24 and 25. In the near-end and far-end cross talk, figure 26 and 27, the peaks and nulls share

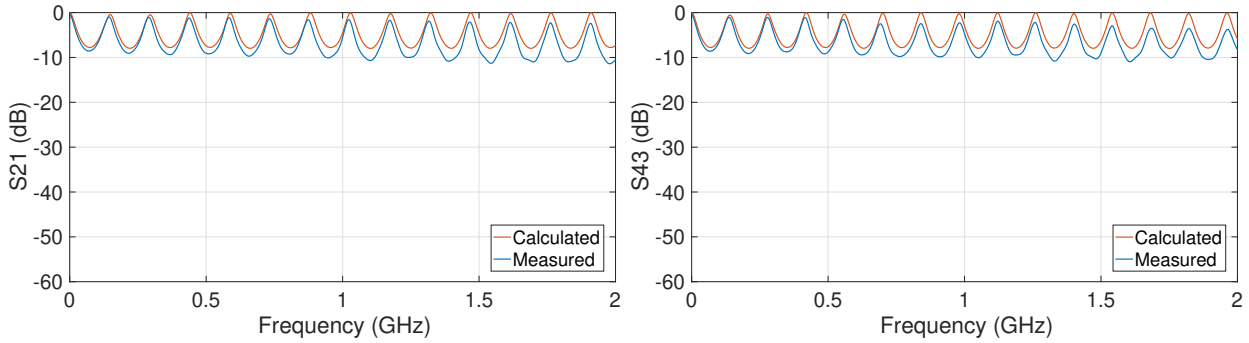

Figure 25: Transmission coefficients for branched line configuration

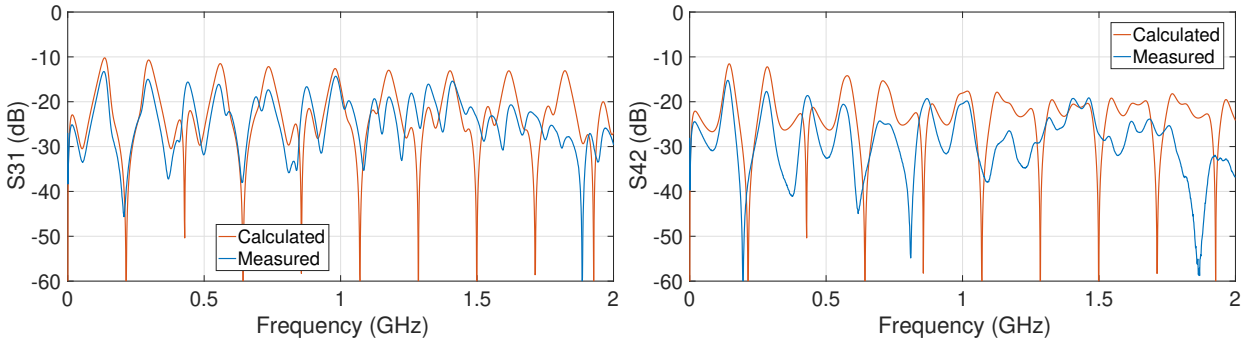

Figure 26: Near-End Cross Talk for branched line configuration

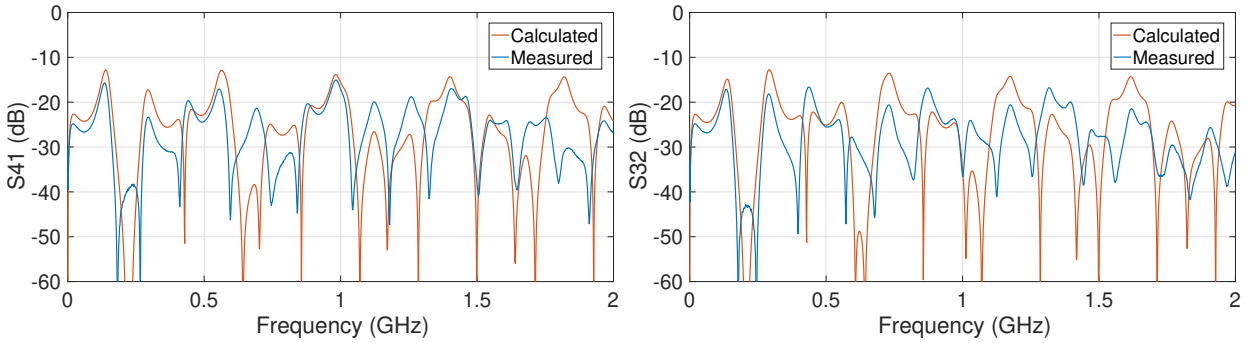

Figure 27: Far-End Cross Talk for branched line configuration

similar trends, but have some disagreement at higher frequencies. There is again a decay in the measured transmission coefficient that is due to the ohmic and radiation losses being neglected in the transmission line model. Overall, this is a satisfying result, indicating the finite element method code is properly calculating the per-unit-length parameters and the transmission line model is properly calculating the voltages and currents along the line.

4.2 Reverberation Chamber

In this electromagnetic susceptibility portion of the study, reverberation chambers were used to measure the radiation from a transmission line structure. Measuring the field levels produced by an excited transmission line and averaging the magnitude squared transmission coefficient over many independent tuner positions gives a signal level proportional to the total power radiated by the transmission line structure. This can be directly compared to

Table 1: Dimensions, in meters, of the reverberation chambers used

Dimension	SMART-80	Small Chamber
Length	13.40	2.13
Width	6.10	0.80
Height	4.80	1.20

the radiation of a wideband horn antenna in the same environment.

There were two separate reverberation chambers used in this study. The dimensions of both chamber is given in table 1. The smaller reverberation chamber was custom-built by our lab. It is made of steel and has a z-fold tuner oriented vertically at one end of the chamber. A study conducted in [10] shows the expected Rayleigh statistics of a properly stirred reverberant cavity is achieved down to 1 GHz for this chamber. The SMART-80 reverberation chamber is commercially produced by ETS-Lindgren. It's made of stainless steel and includes two z-fold tuners, one oriented vertically and one oriented horizontally at opposite ends of the chamber. The tuners can be rotated synchronously or independently, allowing for operation down to 80 MHz.

In this section, a series of experiments was performed in these reverberation chambers to help understand the radiating mechanisms of transmission line circuits. For all of these measurements, one side of the transmission line circuit was being driven while the other was terminated at 50 Ω loads. The radiation from each transmission line structure was measured using a dual-ridge horn antenna in the reverberant field.

4.2.1 SMART-80 Experiments

In this section, we will look at the first set of tests that took place in the SMART-80 reverberation chamber and used the same structure as described in section 4.1 and shown in figure 17. Unlike in section 4.1, during these measurements, the conductors were traded for 24-guage insulated copper wire to allow for a twisted pair configuration. Figure 28

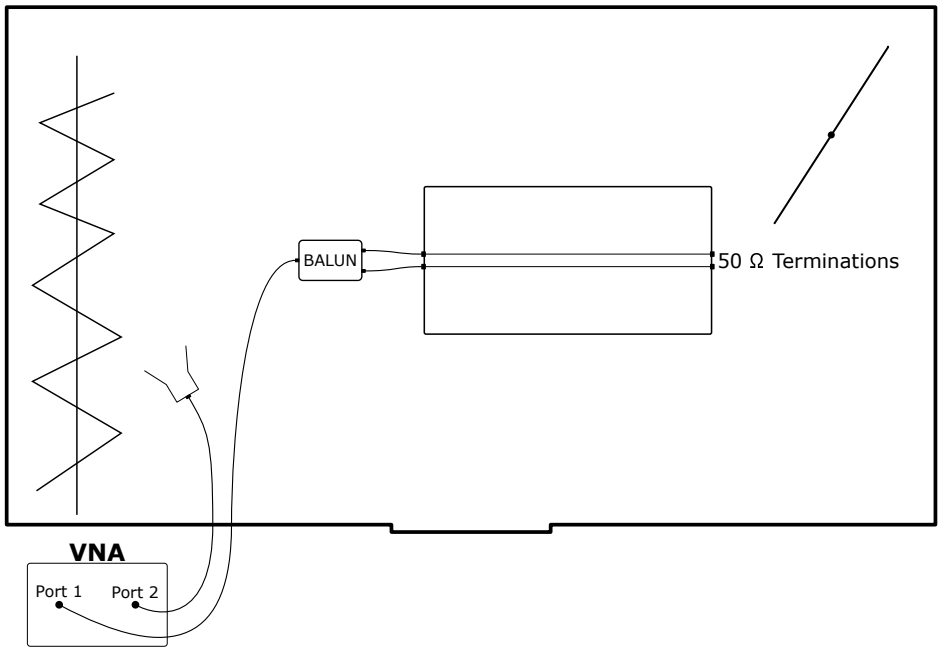

Figure 28: Twin-lead test setup in the SMART-80 reverberation chamber.

shows this structure, configured with a twin-lead line, placed in the SMART-80 chamber. The transmission line structure was placed in the center of the SMART-80 reverberation chamber, one side of the transmission line was driven by a balun or coaxial line, and a dual-ridge horn was used to measure the radiation into the chamber. These measurements were averaged over 100 independent tuner positions.

Single Wire Transmission Line

The first test configuration is shown in figure 29. This structure has a single conductor over a ground plane being terminated in a 50 Ω load. The conductor was 10 cm above the ground plane. This line was being driven by a coaxial transmission line, and was operating in an unbalanced mode.

The radiation from this single wire configuration is being shown in figure 30 compared to a horn-antenna. For this reference horn antenna measurement, the transmission line structure was replaced by a dual-ridge horn antenna and the radiation levels were measured in an identical manner. The horn antenna has a lowest operating frequency of 700 MHz, hence the

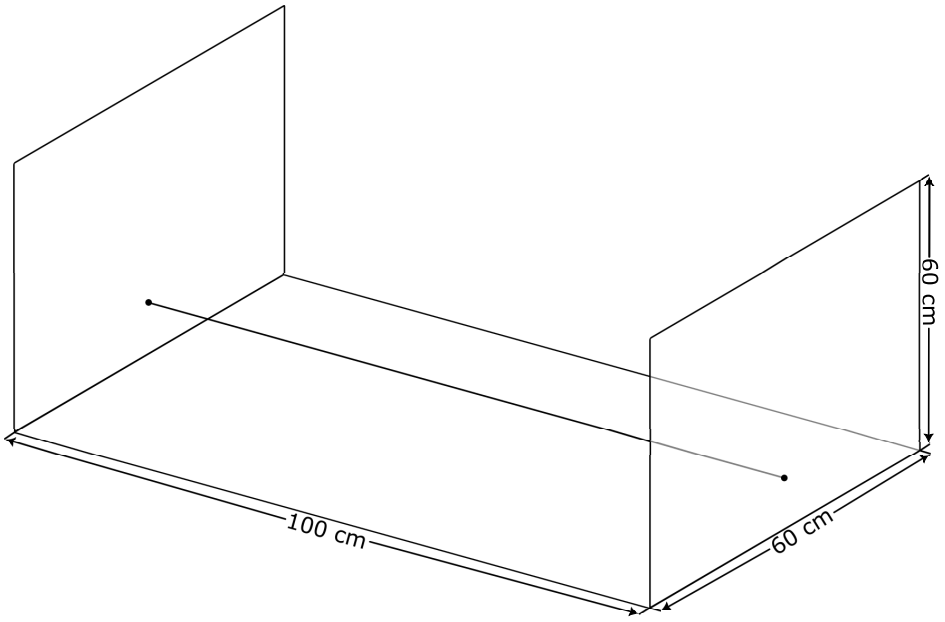

Figure 29: Single wire test setup. There is a 10 cm height above the ground plane

steep drop in radiation bellow that point. The radiation from the single wire configuration is quite high. The line radiation is only 7 dB below the horn antenna at 700 MHz and increases to nearly the same level as the horn antenna at 8.5 GHz. This data seems to indicate the antenna was operating as a wire antenna in this test. The steep drop below 700 MHz is an artifact of the dual-ridge horn used for as the measurement device. This will be quite consistent across all radiation measurements.

Twin-lead and Twisted Pair Transmission Lines

The next test case in the SMART-80 chamber was a twin-lead structure, shown in figure 31. The conductors had a spacing of 1 cm and were 10 cm above the ground plane. This structure was driven by a balun connected to both conductors on the near side, and the far side connectors were terminated in 50 Ω loads to the end plates. The balun was connected to the bulkhead connectors by equal length 50 Ω coaxial transmission lines. This provided a balanced signal on the transmission line structure. A full diagram of this configuration placed in the reverberation chamber is shown in figure 28. It is expected that the radiation

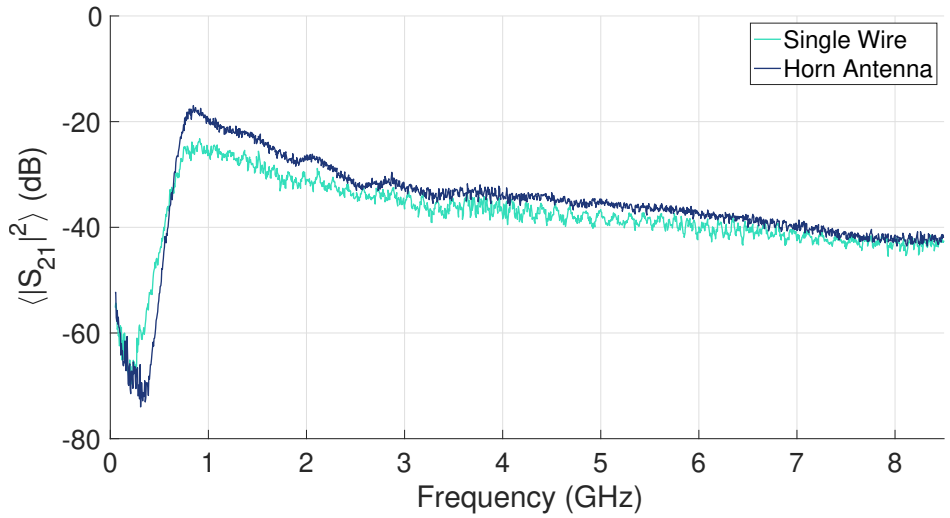

Figure 30: Single wire SMART-80 radiation compared against the dual-ridge horn

from this balanced structure will be less than the unbalanced single conductor from before.

A third test configuration replaced the twin-lead line with a twisted pair from a Cat5 Ethernet cable. Still 10 cm above the ground plane, driven by the balun, and terminated in 50 Ω loads. This configuration can be seen in figure 32. The twisted pair was also driven on one side by a balun and equal length coaxial leads, providing balanced operation. Due to averaging through the twists on the line, it's expected the twisted pair will present even less radiation than the twin-lead line.

The results from the twin-lead and twisted pair radiation measurements are compared to the dual-ridge horn antenna in figure 33. The radiation from this structure is lower than that of the single conductor line, but it is still high, being 20 dB below the horn antenna at 700 MHz and increasing to around 5 dB at 8.5 GHz. The radiation from both conductor assemblies are quite similar over the frequency range, with the radiation of the twisted pair actually exceeding the twin-lead by up to 5 dB from 3.7 GHz to 6.8 GHz.

The results show strong radiation from the balanced two-conductor test configurations. More surprisingly, the twisted pair radiation levels exceed the twin-lead line from 3.7 GHz to 6.8 GHz and nearly matches at all other measured frequencies. This suggests the radiation is not controlled by leakage from the line, and there must be another radiation mechanism

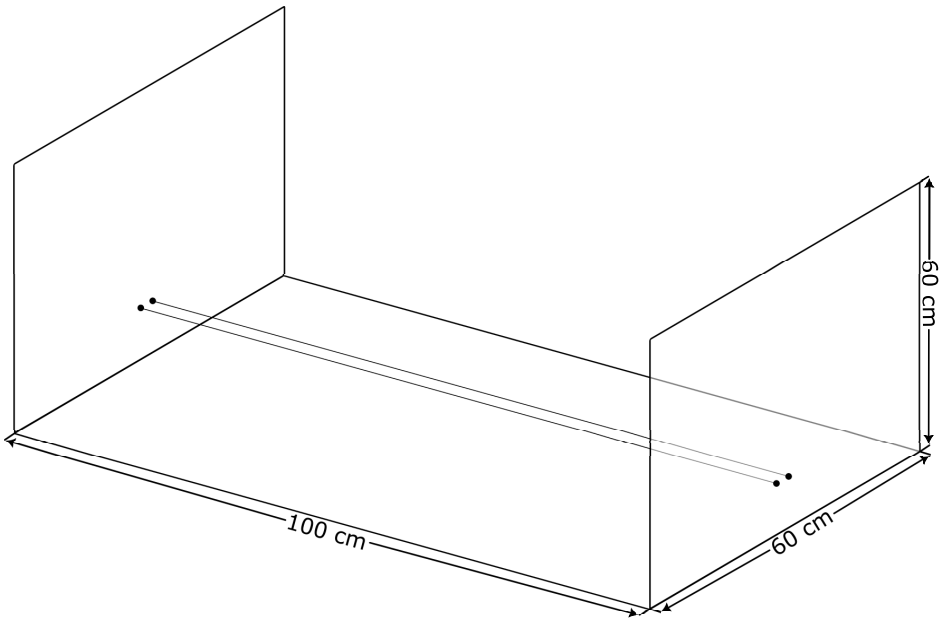

Figure 31: Twin-lead test setup. There is a 10 cm height above the ground plane

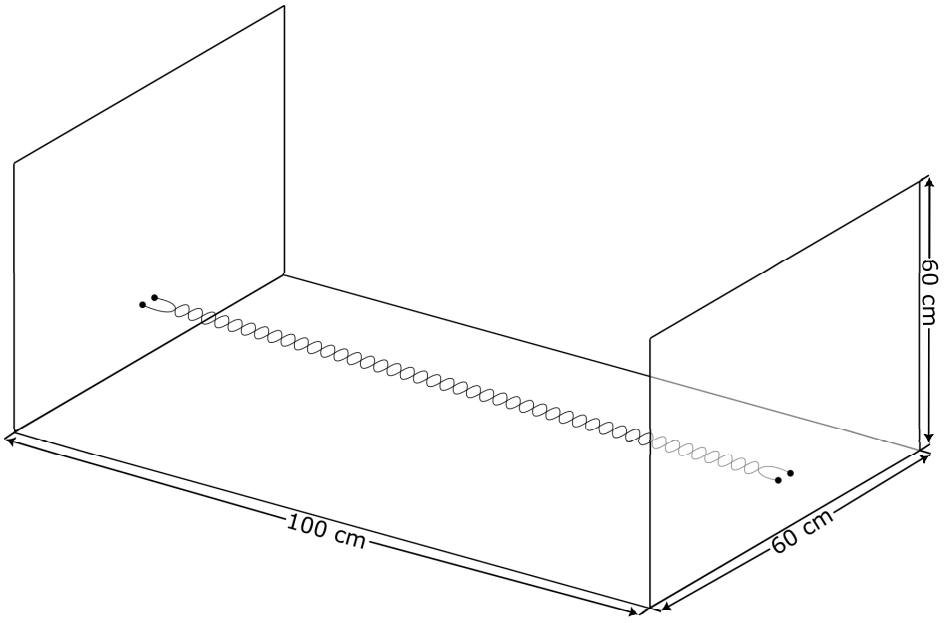

Figure 32: Twisted pair test setup. There is a 10 cm height above the ground plane

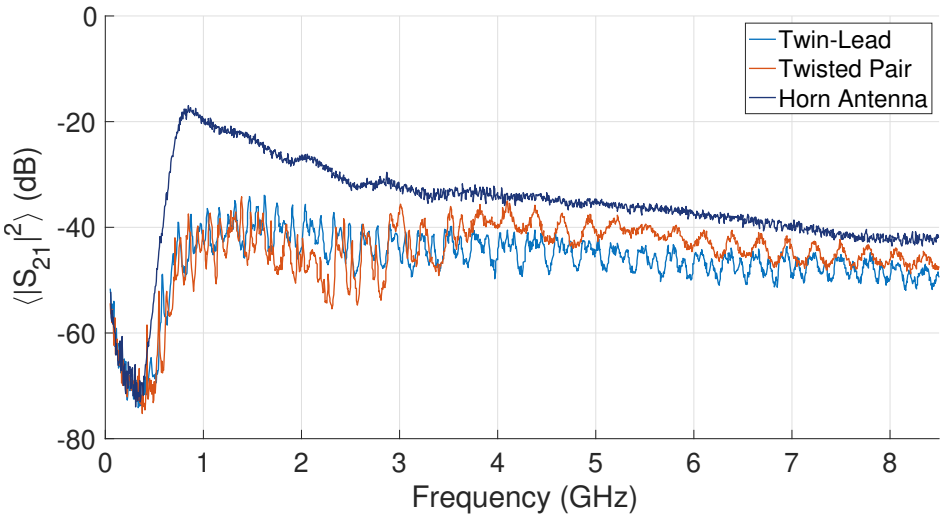

Figure 33: Twin-lead and twisted pair SMART-80 radiation compared against the dual-ridge horn

dominating the radiation losses. This is further examined in the small chamber tests, where areas of interest can be isolated.

4.2.2 Small Chamber Experimental Setup

In this section, experiments were conducted in the small reverberation chamber. Again, a dual-ridge horn antenna was used to measure the radiation from the transmission line structure and 24-guage insulated copper wire was used. These measurements were used to help isolate portions of the test configuration and explore what is dominating the radiation. The reference horn radiation levels are different from the levels observed in the SMART-80 chamber. This is due to a different chamber quality factor and volume. For this work, the relative levels of radiation from the transmission line compared to the reference horn antenna are being analyzed.

SMA bulkhead feeds

The first configuration tested had a two-conductor transmission line structure fed through the chamber walls by SMA bulkhead connectors. It ran along the short axis, spanning 80

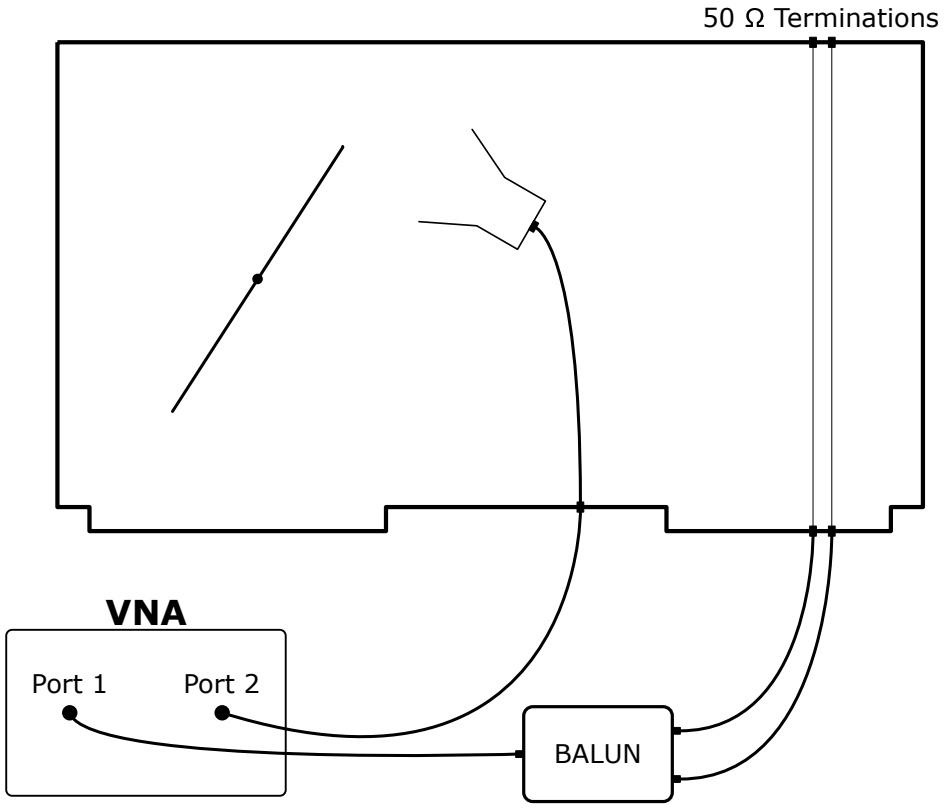

Figure 34: Twin-lead measurement configuration. Conductor spacing of 1 cm.

cm. The conductors were 33 cm from the side wall, and 0.6 m above the floor of the chamber. The transmission line was fed with a balun and terminated in 50 Ω loads to the chamber walls, giving balanced mode operation. These tests were run with both a twin-lead and a twisted pair line in place. The twin-lead configuration shown in figure 34 had a conductor spacing of 1 cm.

Figure 35 shows the twin-lead and twisted pair radiation when fed by SMA bulkhead connectors. The mean radiation has slightly decreased from the SMART-80 test configurations, and the twisted pair radiation is much closer to the twin-lead radiation in this test case. However, they are still quite high. Being 25 dB below the horn antenna at 700 MHz and -10 dB at 8.5 GHz.

These test configurations moved the hardware needed to drive the transmission line, balun and multiple coaxial leads, outside the chamber. It also replaced the open supporting

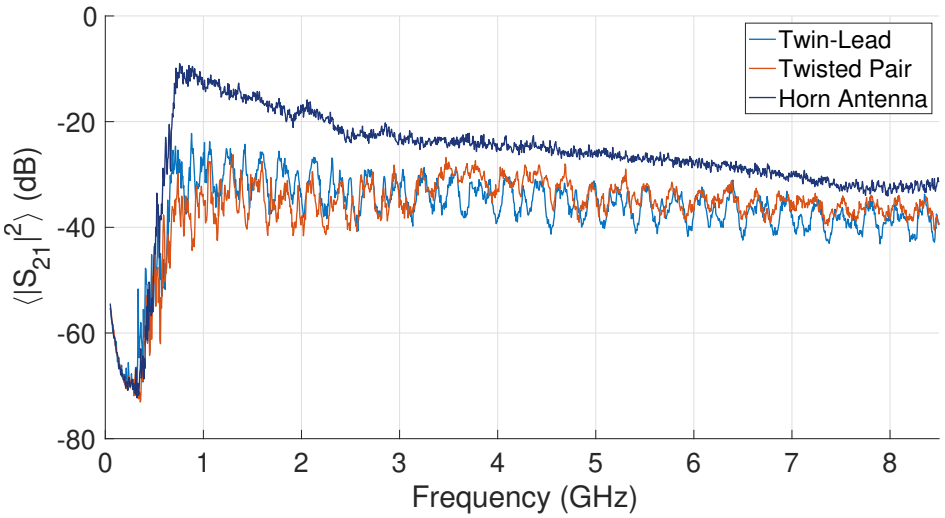

Figure 35: Radiation from twin-lead and twisted pair configurations with SMA bulkhead wall penetrations.

structure with a closed chamber to better approximate wall penetrations in a cavity. This had little effect on the radiation levels measured, indicating something still inside the test volume is continuing to dominate the radiation.

Aperture Pass Through

The next configuration measured replaced the SMA bulkheads with small apertures for the wires to penetrate the walls. This can be seen in figure 36 with the twin-lead line. Using apertures to feed the chamber removes any discontinuity added by the SMA connectors in the reverberant field. The conductors were fed and terminated at small plates outside the chamber. These plates are electrically connected to the chamber body as shown in the diagram. The conductors are again fed by a balun and terminated in 50 Ω loads. Figure 37 shows the twisted pair being passed through the wall of the reverberation chamber. The conducting tape was used to minimize the size of the aperture opening. This test was run with a twin-lead and twisted pair configuration.

The results of these tests are shown in figure 38. The radiation levels have significantly decreased from the levels observed with the SMA bulkhead feeds. The twin-lead is now

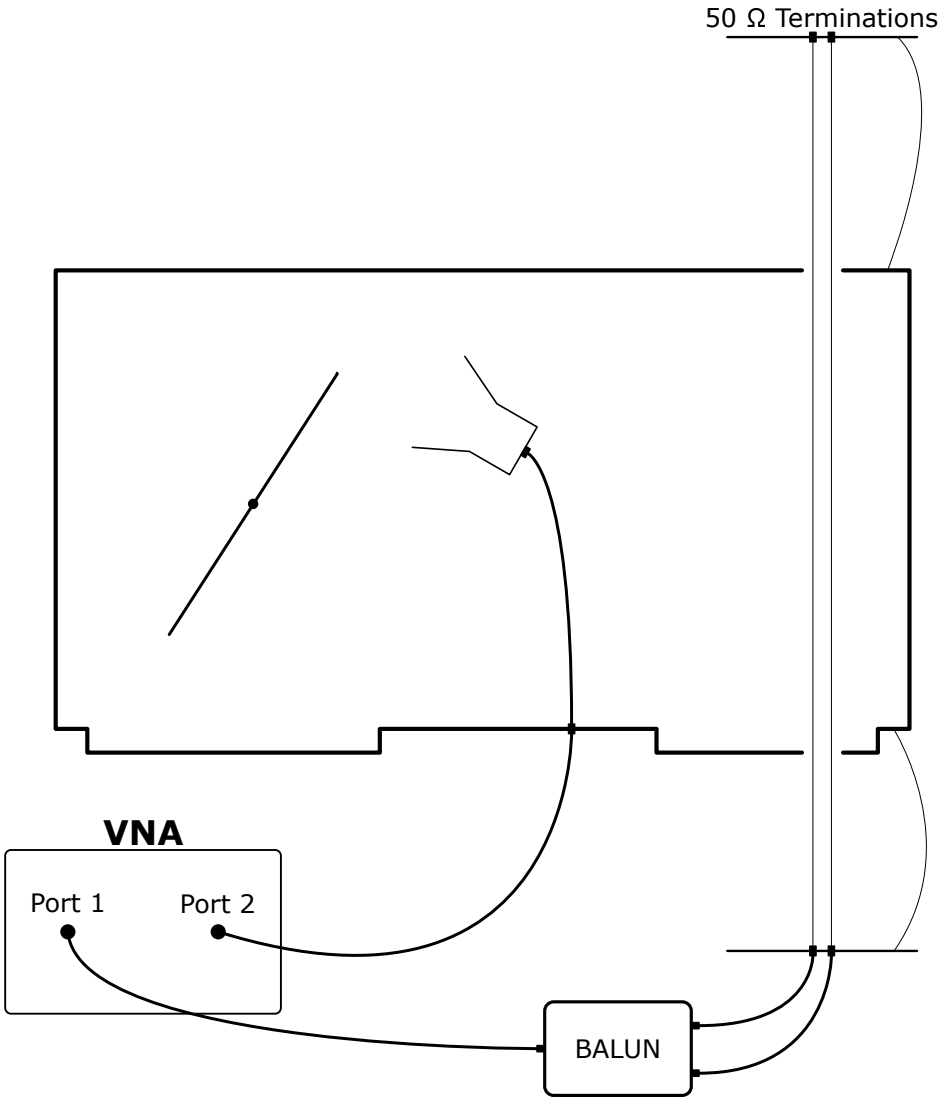

Figure 36: Twin-lead measurement configuration using apertures for wall penetrations.

Figure 37: Twisted pair passed through small reverberation chamber wall.

40 dB below the horn antenna at 700 MHz and 20 dB below the horn antenna at 8.5 GHz. The twisted pair is even lower, -55 dB at 700 MHz and -25 dB at 8.5 GHz when compared with the reference horn antenna.

The 20 to 30 dB decrease in radiation levels shows a trend closer to what was expected throughout the entire experimental phase. The 5 to 15 dB difference in the twin-lead and twisted pair configurations also agrees better with transmission line theory. This data indicates the connectors have been dominating the radiating mechanisms. More tests were conducted to further confirm these results.

Mixed Terminations

The third configuration measured with the small chamber was a mixture of the previous two configurations with one side of the transmission line being terminated at SMA bulkhead feeds and the other side being passed through an aperture and terminated at an external plate. Figures 39 and 40 show both the configuration for feeding a twin-lead line at the

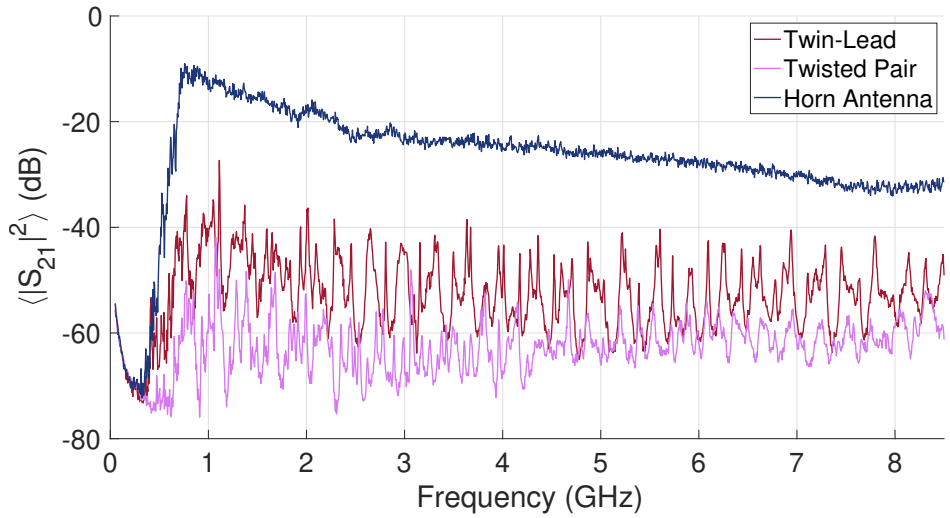

Figure 38: Radiation from twin-lead and twisted pair configurations with aperture wall penetrations.

chamber wall and feeding the line at an external plate while passing through the chamber wall.

The radiation from the twin-lead with mixed terminations can be seen using both feed methods in figures 41. Notice the radiation levels have jumped considerably from the test configuration with only aperture feeds. Both feed methods are 20 dB below the reference horn antenna at 700 MHz. Feeding at the SMA bulkhead wall penetration is 10 dB below the horn antenna at 8.5 GHz while feeding at the external plate is 20 dB below the reference at 8.5 GHz.

Figure 42 shows the radiation from the twisted pair configuration with mixed terminations. These show decreased levels compared to the twin-lead configuration, but still much higher than compared to the aperture feeds. The SMA feed is 30 dB below the reference horn at 700 MHz and 10 dB below at 8.5 GHz. The external plate feed is also 30 dB below at 700 MHz and 20 dB below the reference horn at 8.5 GHz.

When comparing the data from feeding at the SMA bulkhead connectors in figures 41 and 42 with the results from the SMA bulkhead feeds in figure 35, there was not a significant decrease in radiation levels. This seems to indicate that a large portion of the energy being

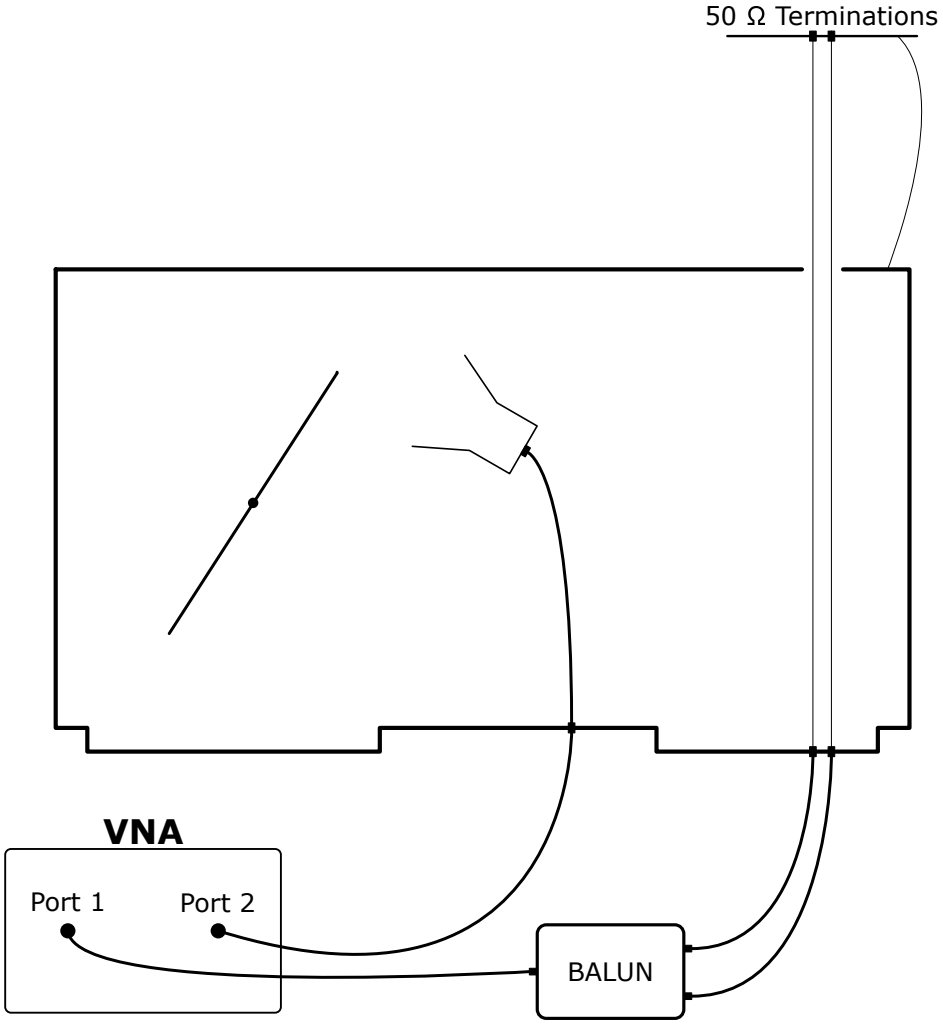

Figure 39: Twin-lead configuration driving at the chamber wall.

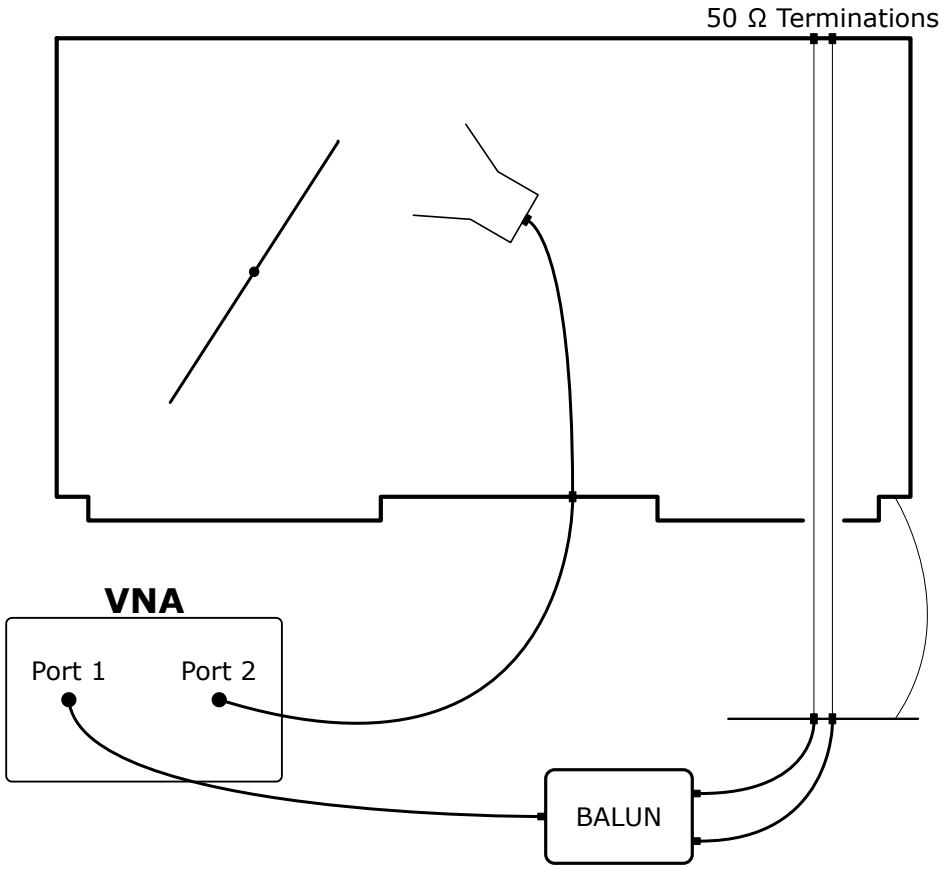

Figure 40: Twin-lead configuration driving at the external plate.

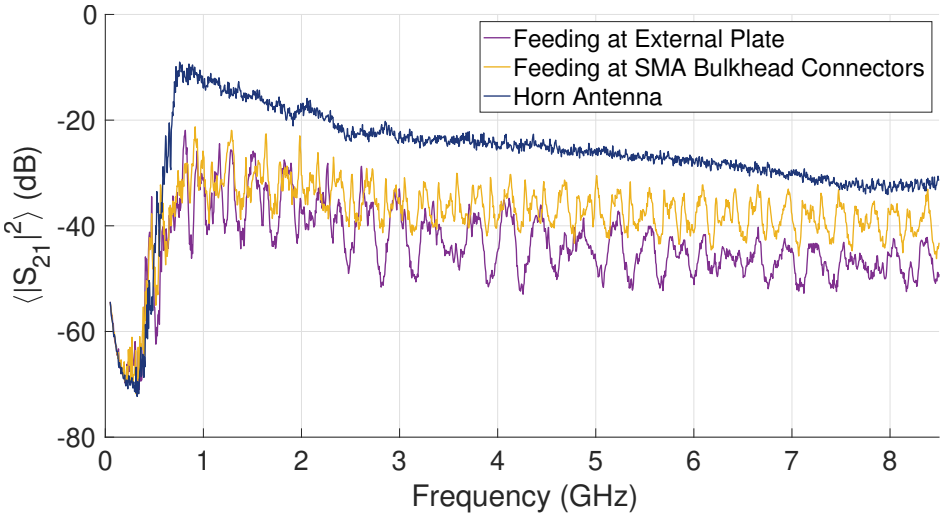

Figure 41: Radiation from the twin-lead configurations with mixed feed methods.

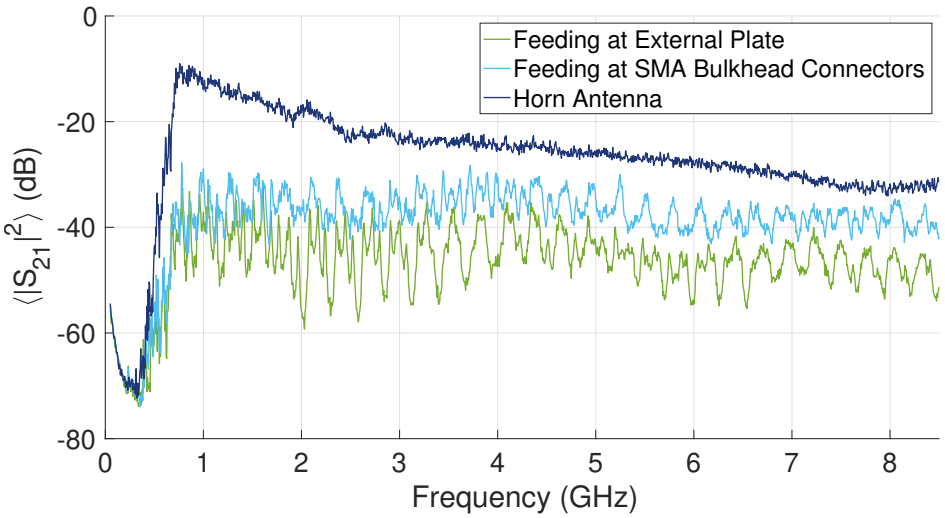

Figure 42: Radiation from the twisted pair configurations with mixed feed methods.

radiated happens at the first set of connectors.

Only Connectors

In an attempt to isolate radiation from only the SMA feeds, the last configuration in the small chamber tests was an experiment run with no conductors in place and only the SMA bulkhead feeds in the wall of the chamber, as shown in figure 43. The connectors were 1 cm apart and being driven by the balun. The connectors in the far wall remained in place and were terminated in 50 Ω loads. Figure 16 shows the SMA bulkhead feeds used for this test.

The radiation from only SMA bulkhead feeds is compared to the reference horn antenna in figure 44. The radiation at 700 MHz is quite near the noise floor, being 68 dB below the reference antenna. As the wavelength decreases, the radiation from the connector assembly quickly increases to only 5 dB below the dual-ridge horn antenna at 8.5 GHz.

As the length of the feed pins grow larger compared to the wavelength, the radiation into the chamber becomes larger as well. From this data, it seems these connectors are acting as efficient antennas, and matching very well to this stirred field. This means as the field is being stirred through tuner positions, the connectors are cycling through periods of large radiation and little radiation. This result averages to show large radiation from the

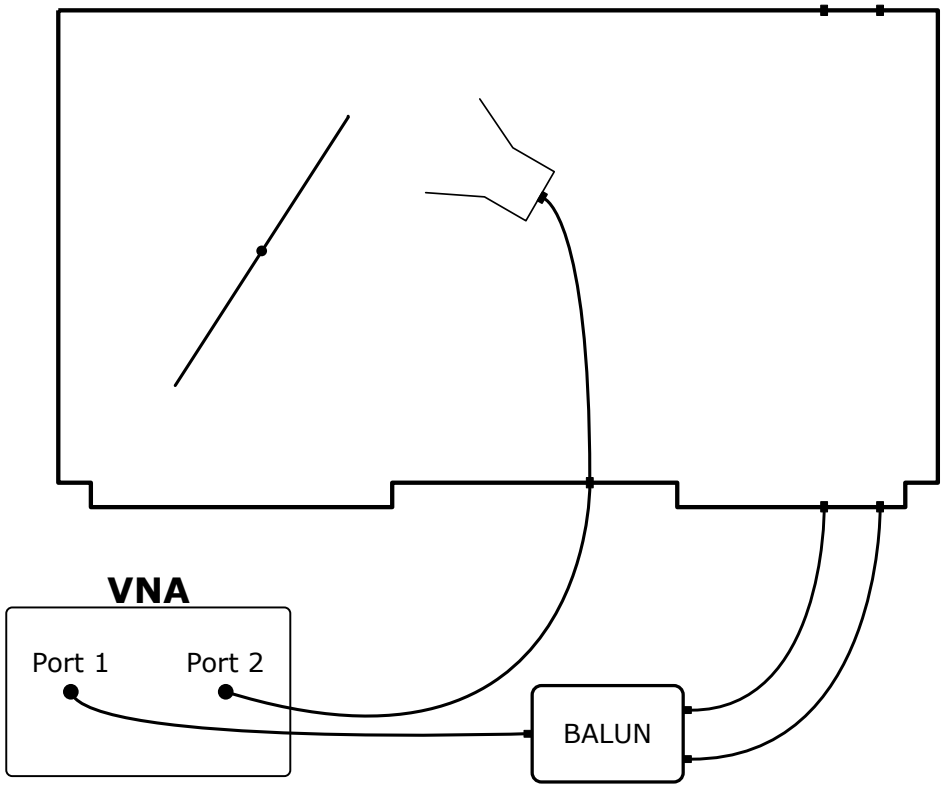

Figure 43: SMA bulkhead configuration without conductors in place.

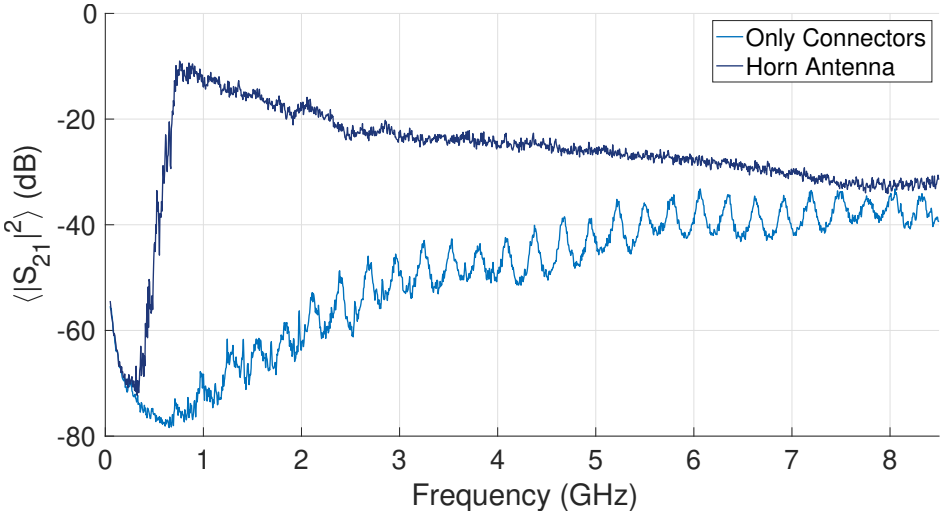

Figure 44: Radiation from only the SMA bulkhead feeds.

connectors. Interestingly, the radiation levels from 7-8.5 GHz match very closely to the levels seen with a conductor in place

4.2.3 Nested Cavity Experimental Setup

The final set of experiments was conducted by placing the small chamber inside the SMART-80 chamber, giving a nested cavity arrangement. With this setup, radiation from the transmission line was measured inside the small chamber and inside the SMART-80. This allowed for the radiation levels of two separate areas of interest to be viewed and compared simultaneously. Unfortunately, because the differing volumes and quality factors in the separate cavities, the radiation measurement data must be adjusted for proper comparison and will have little correlation to previous results. By correcting for reflection losses, input power, and differing chamber properties, shown in equation (4.2.1), and outlined in [5], the data can be compared using an adjusted relative power level radiated by the transmission line structure being observed.

$$P_t = \frac{16\pi^2 V}{\lambda^3 Q} \frac{\langle |S_{21}|^2 \rangle}{(1 - |\langle S_{11} \rangle|^2)(1 - |\langle S_{22} \rangle|^2)} \tag{4.2.1}$$

SMA Bulkhead Feeds

Much like in section 4.2.2, SMA bulk head connectors were placed in the walls of the small reverberation chamber and 24-guage insulated copper wire was stretched between them to form the transmission line. The line was fed by a balun on one side and terminated in 50 Ω loads on the other, establishing a balanced mode signal. The twisted pair configuration for radiation in the small chamber and in the SMART-80 chamber can be seen in figures 45 and 46 respectively.

The relative power levels of the twin-lead test configuration can be seen in figure 47. At 700 MHz there is 20 dB less radiation in the SMART-80 chamber than in the small reverberation chamber and there is 25 dB less at 8.5 GHz. Notice at 3 GHz, there is a

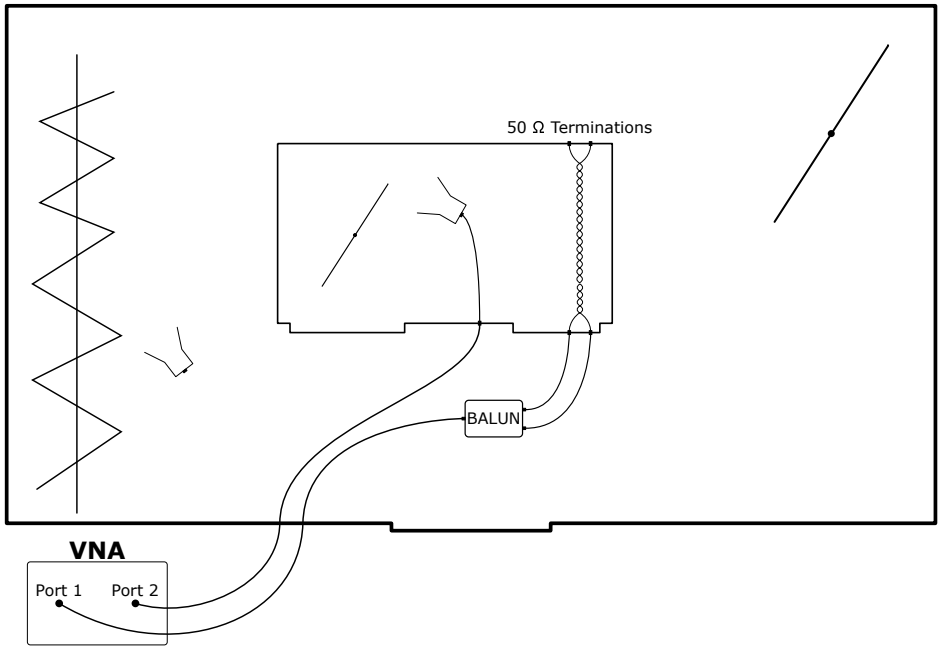

Figure 45: Twisted pair, SMA feed configuration. Measuring radiation in the small chamber.

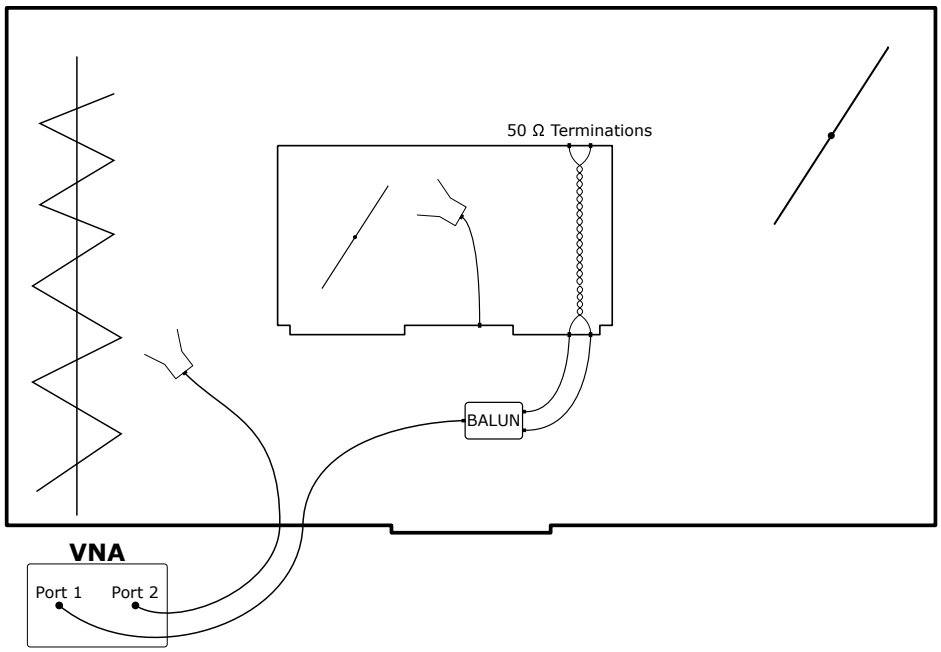

Figure 46: Twisted pair, SMA feed configuration. Measuring radiation in the SMART-80.

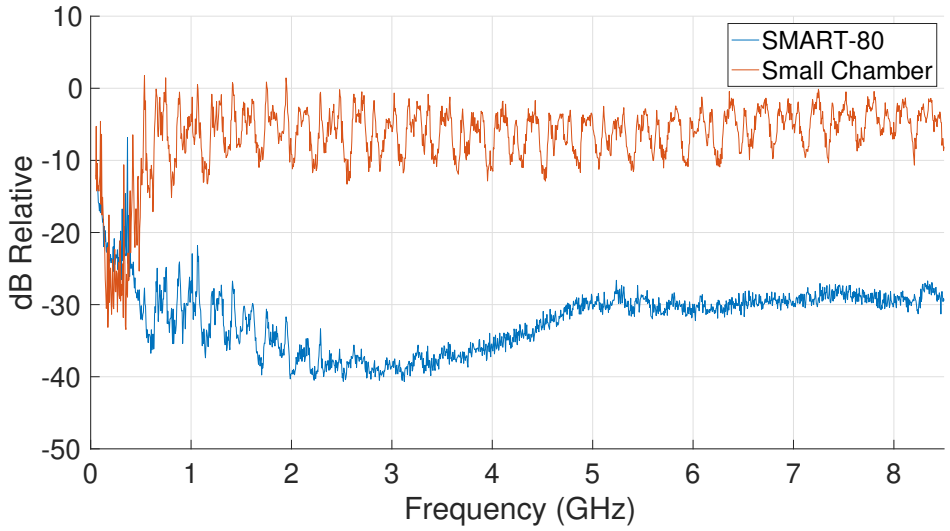

Figure 47: Relative radiated power of the twin-lead line with SMA bulkhead feeds in the nested chambers.

maximum of 35 dB difference in the radiation levels.

Similar results for the twisted pair are shown in figure 48. The SMART-80 radiation is 20 dB below the small chamber radiation at 700 MHz. SMART-80 radiation is 30 dB lower at 3 GHz and 25 dB lower at 8.5 GHz when compared to the small chamber radiation.

These results indicate there is very little radiation from the feeding elements – adapters, balun, and coaxial leads – and the bulk of energy was transferred onto the transmission line.

Aperture Pass Through

The final measurement configuration was similar to that described in section 4.2.2. The transmission line was fed through the walls of the chamber and terminated with SMA connectors at external plates. It was fed by a balun and terminated in 50 Ω loads, giving balanced operation. Figures 49 and 50 show the measurement scenarios.

Figure 51 shows the radiated power into the SMART-80 and small reverberation chambers from the twin-lead transmission line structure when terminated at the external plates. The mean power radiated into the small chamber is 18 dB below the power radiated into the SMART-80 at 700 MHz and is 12 dB below at 8.5 GHz.

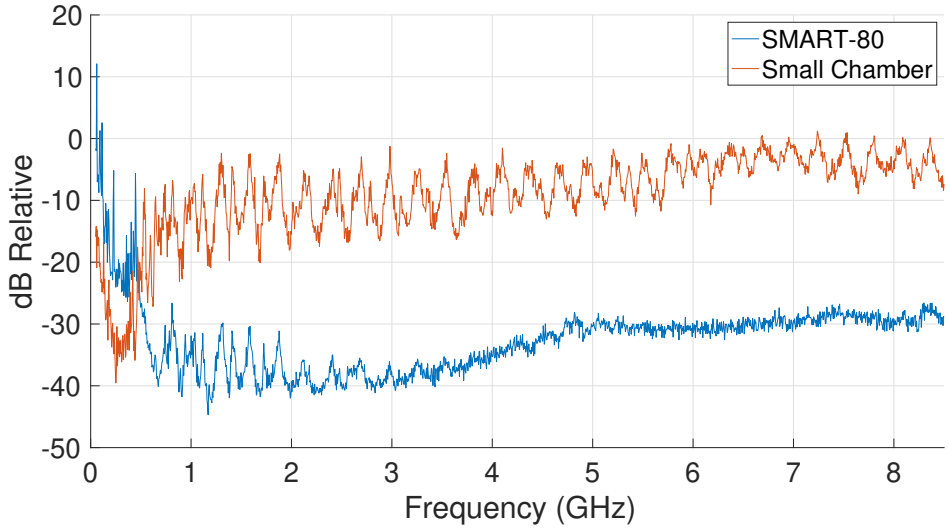

Figure 48: Relative radiated power of the twisted pair line with SMA bulkhead feeds in the nested chambers.

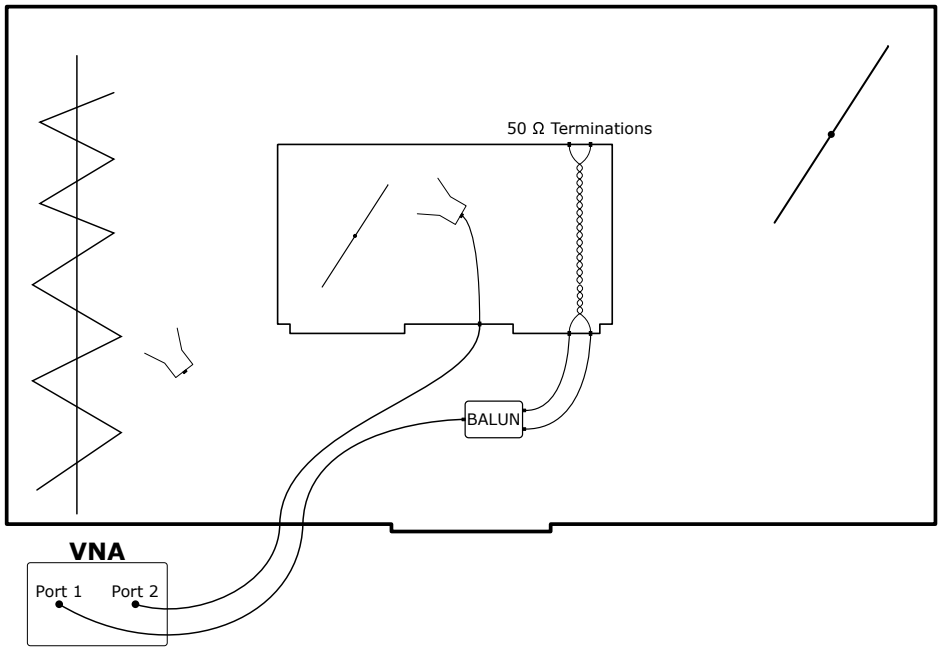

Figure 49: Twisted pair, SMA feed configuration. Measuring radiation in the small chamber.

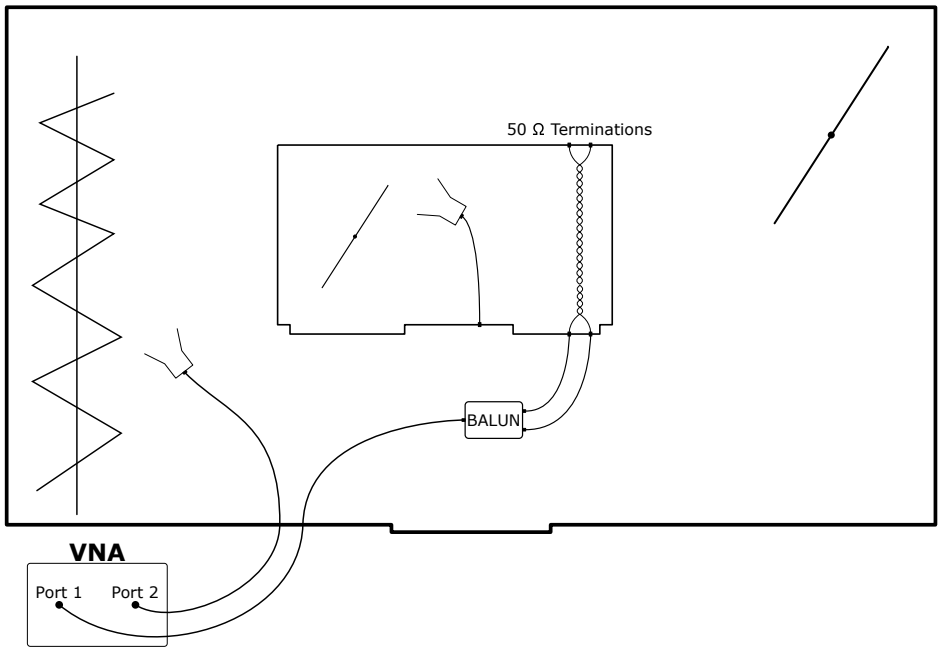

Figure 50: Twisted pair, SMA feed configuration. Measuring radiation in the SMART-80.

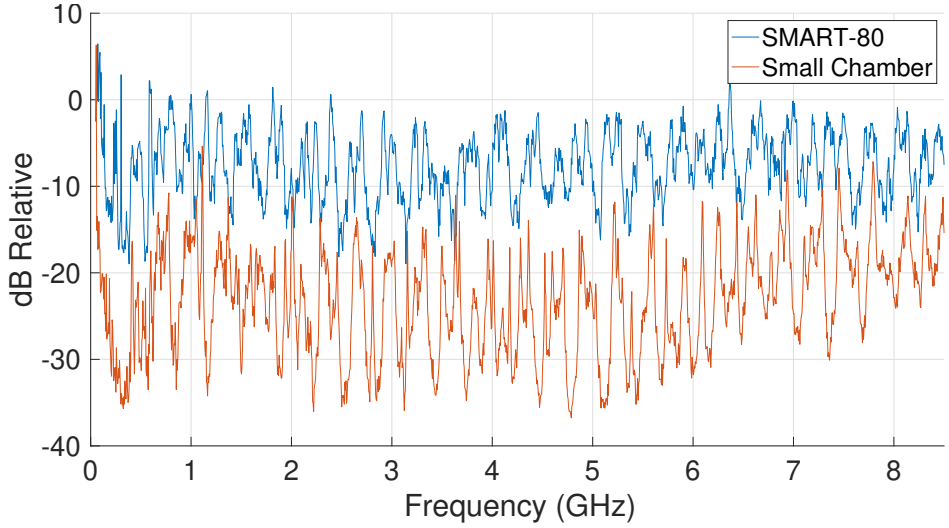

Figure 51: Relative radiated power of the twin-lead line with aperture feeds in the nested chambers.

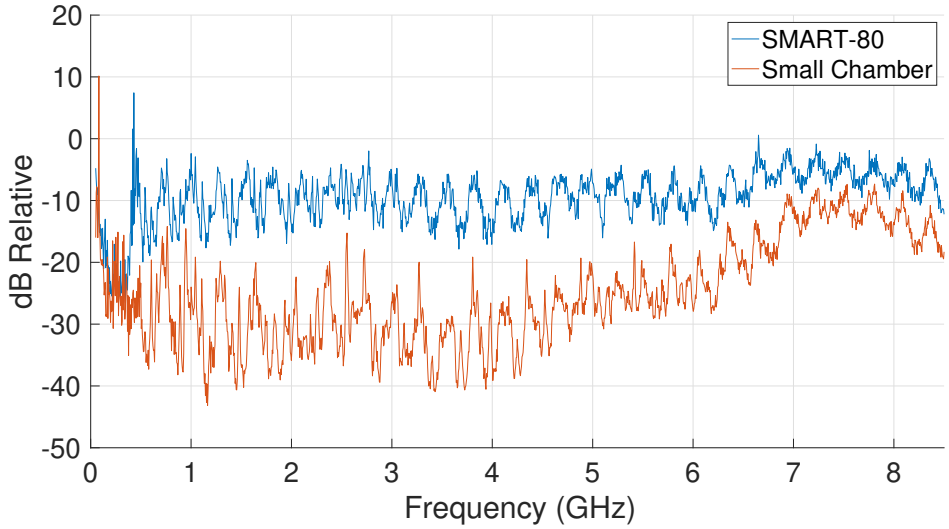

Figure 52: Relative radiated power of the twisted pair line with aperture feeds in the nested chambers.

The test results for the twisted pair terminated in the external plates is shown in figure 52. The small chamber power levels are 20 dB lower than the SMART-80 power levels at 700 MHz and 8 dB lower than the SMART-80 power levels at 8.5 GHz.

For both the twin-lead and twisted pair configuration, when the SMA bulkhead connectors are inside the small chamber walls, the radiation in the SMART-80 chamber is much lower than in the small chamber. When the SMA connectors are moved to the external feed plates, the radiation in the SMART-80 chamber jumps dramatically and the radiation in the small chamber drops. These results from the nested cavity experiments help to further emphasize that the radiation is being dominated by the discontinuity at the terminations and not by leakage from the transmission line. It also shows that the balun, coaxial leads, and adapters are not significantly contributing to the radiation.

CHAPTER V

Conclusion

5.1 Discussion

During this study, the mode stirred reverberation chamber has proven to provide an environment that is highly suited to the measurement of total power levels radiated by the transmission line geometries considered. Averaging the magnitude-squared scattering parameter over numerous tuner steps yields a signal level proportional to the total power radiated by that structure, which can be directly compared to the radiation by a wideband horn antenna. By placing various segments of the transmission line itself and the elements used to provide a balanced feed within(or external to) the chamber cavity, the relative contributions to radiated power from each component can be directly measured. Radiation pattern effects are removed by averaging over the tuner positions.

The measurements indicate that the termination of the transmission lines at the SMA bulkhead connectors are the strongest contributor to the radiated emissions at the frequencies considered in this paper. The strongest radiation was consistently measured when both ends of the transmission lines were terminated in connectors that were exposed to the reverberation chamber cavity, mounted either on a plate within the large chamber or mounted on the walls of the small chamber itself. The total emissions did not strongly depend on the transmssion line type when the connectors were exposed to the internal cavity, indicating that the leakage from the lines themselves was weaker than the termination radiation. This conclusion is further supported by the measured emissions when only one side of the line was fed by bulkhead connectors and the other side was terminated in a plate outside the

small chamber. The emissions within the cavity reduced only slightly when the feed side of the line was terminated inside the chamber but reduced more so when only the far side of the line was terminated inside the chamber. This shows much of the power placed on the line had already been radiated before it reached the far-side connectors. This behavior is consistent with the observations in [3], who noted that emissions from a shielded line whose shield is attached to a connector through a pigtail can be equal to the radiation from an unshielded line.

Minimum emissions into the cavity were observed when the transmission lines were routed continuously through apertures in the small reverberation chamber walls. This configuration isolated the SMA feed connectors, balun, and feed plate structures from the chamber cavity. Radiation in this case was due to leakage of the lines themselves or perhaps from currents induced on the chamber walls through reactive coupling to the line conductors. In this case, emissions were lower with the twisted-pair line than with the twin-lead line in this case as expected from transmission line theory.

In the nested cavity experiments, radiation from the SMA feed connectors, balun, and feed plate structures was isolated from the radiation by the transmission line while being simultaneously measured. This further supported the conclusion that radiation is being dominated by the termination of the transmission line. When the feed structure was placed in the walls of the small chamber, the measured emission in the small chamber greatly exceed the emissions in the SMART-80. However, when the feed structure is placed in the SMART-80, the measured emissions in the SMART-80 exceed that in the small chamber.

5.2 Future Work

The experimental results suggest two areas for future work. The first is to make some direct comparisons between measured radiation results and predicted results, from the Clayton R. Paul model and also some other models outlined in II. This will provide reference between the results and possible models to represent it. There could also be value in performing some

frequency domain reflectometry and time domain reflectometry measurements. This would provide insight into locations of faults, possible locations of high radiation, along the line. Then, tests could be designed to isolate those areas to further investigate their radiation properties.

REFERENCES

[1] Y. Bayram and J.L. Volakis, *A generalized mom-spice iterative technique for field coupling to multiconductor transmission lines in presence of complex structures*, IEEE Transactions on Electromagnetic Compatibility **47** (2005), no. 2, 234–246.

[2] T. Steinmetz H. Haase, J. Nitsch, *Transmission-line super theory: A new approach to an effective calculation of electromagnetic interactions*, URSI Radio Science Bulletin **2003** (2003), no. 307, 33–60.

[3] F. Han, *Radiated emission form shielded cables by pigtail effect*, TEMC **34** (1992), no. 3, 345–348.

[4] F. Hecht, *New development in freefem++*, Journal of Numerical Mathematics **20** (2012), no. 3-4, 251–265. MR 3043640

[5] D. A. Hill, *Electromagnetic fields in cavities: Deterministic and statistical theories*, Wiley, Hoboken, New Jersey, 2009.

[6] M. Klingler P. Besnier, S. Chabane, *Some limiting aspects of transmission line theory and possible improvements*, IEEE Electromagnetic Compatibility Magazine **3** (2014), no. 2, 66–75.

[7] C. R. Paul, *A comparison of the contributions of common-mode and differential-mode currents in radiation emissions*, IEEE Trans. Electromag. Compat. **31** (1989), no. 2.

[8] ———, *Analysis of multiconductor transmission lines*, 2nd ed., Wiley-Interscience, Hoboken, New Jersey, 2008.

[9] M. Klingler S. Chabane, P. Besnier, *Extension of the transmission line theory application with modified enhanced per-unit-length parameters*, Progress in Electromagnetic Research **32** (2013), 229–244.

[10] M. D. Sowell, *The statistical behivor of electromagnetic fields within aperture-coupled nested reverberent cavities*, 2022.

[11] J. E. Storer and R. King, *Radiation resistance of a two-wire line*, Proc. IRE **39** (1951), no. 11, 1408–1412.

[12] J.C. West, C. F. Bunting, and P. G. Bremner, *Common-mode contribution to currents induced on a terminated multiconductor transmission line in a reverberant field*, Proc. 2022 IEEE Int. Symp. Electromag. Compat. (August 1-5, Spokane, Washington), 2022, pp. 344–349.

VITA

Matthew Kyle Roth

Candidate for the Degree of

Masters of Science

Thesis: AN INVESTIGATION INTO TRANSMISSION LINE RADIATION

Major Field: Electrical Engineering

Biographical:

Education:

Completed the requirements for the Masters of Science in Electrical Engineering at Oklahoma State University, Stillwater, Oklahoma in May, 2023.

Completed the requirements for the Bachelor of Science in Electrical Engineering at Oklahoma State University, Stillwater, Oklahoma in May, 2021.